A SPATIALLY ADAPTIVE LERAY-α REGULARIZED FINITE ELEMENT METHOD FOR GEOTACTIC BIOCONVECTION

JIABAO NIE*, CATALIN TRENCHEA†, AND MARTINA BUKAČ‡

Abstract. Accurate long-time simulations of geotactic bioconvection can require prohibitively fine spatial resolution. We develop a spatially adaptive Leray-α regularized finite element method that reduces computational cost while retaining the dominant large-scale dynamics. The method regularizes the advecting velocity in the momentum equation and preserves key properties of the original model, including total microorganism mass conservation and a kinetic–potential energy balance. The time-discrete algorithm combines a one-legged θ-method, an Oseen linearization, and a decoupled subiteration procedure. We establish a semi-discrete stability estimate and prove linear convergence of the subiterations under a time-step restriction. We further analyze the grad-div stabilized adaptive filter used to approximate the Stokes-type filtered velocity. At the continuous level, increasing the grad-div stabilization parameter improves the approximation. At the discrete level, however, we identify a competing divergence-residual effect that limits the benefit of over-stabilization. Numerical experiments, including cases with concentration-dependent viscosity, show that the proposed method captures the dominant dynamics on substantially coarser meshes than the standard finite element method, with a significant reduction in computational cost.

1. Introduction. Geotactic bioconvection describes the macroscopic convective patterns that arise in dense suspensions of free-swimming microorganisms exhibiting negative geotaxis, a preferential upward swimming response against gravity. As the population accumulates near the upper surface, the resulting top-heavy suspension becomes unstable. Concentrated plumes of organisms then descend into the bulk fluid, and the collective dynamics generates large-scale flow patterns that may persist over long times [11, 37]. Bioconvection is relevant to a range of biological and engineering settings, including microbial enhanced oil recovery, large-scale biofuel production [4, 5], wastewater treatment [33], and the design of microfluidic lab-on-a-chip systems [38]. In these applications, understanding long-time dynamics and large-scale flow structures is essential. Accurate simulation of these features requires stable numerical methods that remain reliable over long time intervals.

Bioconvection is closely related to Rayleigh–Bénard thermal convection. In both systems, an adverse density gradient generates buoyancy-driven instability and convective motion, although the physical origin of the density gradient is different. In Rayleigh–Bénard convection, sufficiently large Rayleigh numbers are known to produce weakly turbulent or chaotic flow dynamics [17, 25]. Bioconvection exhibits analogous complexity [39]. It is observed that sufficiently large values of the bioconvective Rayleigh number defined in [11, 16, 35, 36] lead to irregular flow dynamics. This behavior makes the computational approximation of bioconvection especially challenging. Fully resolved simulations may require very fine spatial resolution and can become prohibitively expensive.

These difficulties motivate the development of regularized numerical models that retain the essential large-scale dynamics while reducing computational cost. In this work, we develop a spatially adaptive Leray-α regularized finite element method for geotactic bioconvection. In the following text, we first recall the classical geotactic bioconvection model, then review the Leray-α filtering framework, and finally discuss related numerical methods before summarizing our main contributions.

1.1. Bioconvection model. We first recall the classical geotactic bioconvection model and its basic structural properties. These properties provide the reference point for the spatially adaptive Leray-α regularized model introduced in Section 2.

Let $\Omega \subset \mathbb{R}^d$, $d = 2,3$, be a bounded domain with smooth boundary $\partial\Omega$. Let $c(\boldsymbol{x},t)$ denote the concentration of microorganisms, and let $\boldsymbol{u}(\boldsymbol{x},t)$ and $p(\boldsymbol{x},t)$ denote the velocity and pressure of the culture fluid. The collective dynamics of negatively geotactic microorganisms immersed in a viscous incompressible fluid can be modeled in $\Omega \times (0,T]$ by a coupled system consisting of the Navier–Stokes model and a convective

*Department of Applied and Computational Mathematics and Statistics,University of Notre Dame, Notre Dame, IN, 46556, USA. email: jnie2@nd.edu

†Department of Mathematics, University of Pittsburgh, Pittsburgh, PA, 15260, USA. email:trenchea@pitt.edu

‡Department of Applied and Computational Mathematics and Statistics,University of Notre Dame, Notre Dame, IN, 46556, USA. email: mbukac@nd.edu

transport equation [11]:

$$\begin{aligned}
&\frac{\partial \boldsymbol{u}}{\partial t}(\boldsymbol{x},t) - \nabla\cdot\big(\nu(c(\boldsymbol{x},t))D(\boldsymbol{u}(\boldsymbol{x},t))\big) + (\boldsymbol{u}(\boldsymbol{x},t)\cdot\nabla)\boldsymbol{u}(\boldsymbol{x},t) = -\nabla p(\boldsymbol{x},t) - g\big(1+\gamma c(\boldsymbol{x},t)\big)\boldsymbol{i}_d + \boldsymbol{f}(\boldsymbol{x},t),\\
&\nabla\cdot\boldsymbol{u}(\boldsymbol{x},t) = 0,\\
&\frac{\partial c}{\partial t}(\boldsymbol{x},t) - \Theta\Delta c(\boldsymbol{x},t) + (\boldsymbol{u}(\boldsymbol{x},t)\cdot\nabla)c(\boldsymbol{x},t) + U\frac{\partial c}{\partial x_d}(\boldsymbol{x},t) = 0.
\end{aligned} \tag{1.1}$$

Here, $D(\boldsymbol{u}) = (\nabla\boldsymbol{u} + \nabla\boldsymbol{u}^T)/2$ denotes the symmetric part of the stress tensor, $\boldsymbol{f}$ is a prescribed body force, g is gravitational acceleration , and $\boldsymbol{i}_d = (0,\cdots,1)^T$ is the vertical unit vector. The parameters $\Theta > 0$ and $U > 0$ denote the diffusion coefficient and the mean upward swimming speed of the microorganisms, respectively. The parameter $\gamma > 0$ represents the relative density difference between the microorganisms and the culture fluid, defined as $\gamma = \rho_0/\rho_m - 1$, where ρ_0 and ρ_m are the densities of the microorganisms and the fluid, respectively. The viscosity $\nu = \nu(c)$ may depend on the local concentration [9]. When this dependence is neglected, it reduces to a positive constant. The term $-g(1+\gamma c)\boldsymbol{i}_d$ captures the buoyancy feedback between the microorganism distribution and the fluid motion.

We impose the no-slip boundary condition for the fluid and a no-flux boundary condition for the concentration:

$$\boldsymbol{u} = 0, \qquad \Theta\frac{\partial c}{\partial \boldsymbol{n}} - cUn_d = 0 \qquad \text{on } \partial\Omega\times(0,T], \tag{1.2}$$

where $\boldsymbol{n} = (n_1,\ldots,n_d)$ denotes the exterior unit normal vector on $\partial\Omega$ and n_d is its d-th component.

The system (1.1)–(1.2) has several structural properties [14] that are central to the present work. First, if $c_0 \geq 0$, the continuous concentration remains nonnegative under suitable regularity assumptions. Second, the no-flux boundary condition ensures conservation of the total microorganism mass:

$$M(t) := \int_\Omega c(\boldsymbol{x},t)\,d\boldsymbol{x} = \int_\Omega c_0(\boldsymbol{x})\,d\boldsymbol{x} =: M_0, \qquad t \geq 0.$$

We define the kinetic energy of the fluid flow, and the gravitational potential energy associated with the microorganism distribution by

$$\mathrm{KE}(t) = \frac{1}{2}\int_\Omega |\boldsymbol{u}(\boldsymbol{x},t)|^2\,d\boldsymbol{x}, \qquad \mathrm{PE}(t) = \gamma g\int_\Omega c(\boldsymbol{x},t)(x_d - x_d^{\min})\,d\boldsymbol{x},$$

where $x_d^{\min}$ is the 'bottom' of Ω in the vertical direction. The total energy satisfies the balance

$$\frac{d}{dt}\big(\mathrm{KE}+\mathrm{PE}\big) + \int_\Omega \nu(c)|D(\boldsymbol{u})|^2\,d\boldsymbol{x} = -\gamma g\int_\Omega \Theta\frac{\partial c}{\partial x_d}d\boldsymbol{x} + M_0\gamma g U + \int_\Omega \boldsymbol{f}\cdot\boldsymbol{u}\,d\boldsymbol{x}. \tag{1.3}$$

1.2. Leray-α model and adaptive filtering. Regularization models are widely used to reduce the computational cost of the simulations of incompressible flows. A foundational approach is Leray's regularization [31], in which the advecting velocity in the nonlinear convection term is replaced by a spatially filtered counterpart:

$$\frac{\partial \boldsymbol{v}}{\partial t} - \nu\Delta\boldsymbol{v} + (\overline{\boldsymbol{v}}\cdot\nabla)\boldsymbol{v} + \nabla q = \boldsymbol{f}, \qquad \nabla\cdot\boldsymbol{v} = 0. \tag{1.4}$$

Here $\overline{\boldsymbol{v}}$ denotes convolution of $\boldsymbol{v}$ with a Gaussian kernel of filtering radius $\alpha > 0$. In practice, the Gaussian convolution can be replaced by the Helmholtz filter (also called α-filter):

$$-\alpha^2\Delta\overline{\boldsymbol{v}} + \overline{\boldsymbol{v}} + \nabla\lambda = \boldsymbol{v}, \quad \nabla\cdot\overline{\boldsymbol{v}} = 0 \quad \text{in} \quad \Omega, \qquad \overline{\boldsymbol{v}} = \boldsymbol{v} \quad \text{on} \quad \partial\Omega. \tag{1.5}$$

The Helmholtz filter is an $\mathscr{O}(\alpha^4)$ approximation to the Gaussian filter [15], and computationally more efficient. The interpretation of α remains as the filtering radius. Note that the Navier-Stokes equations are recovered when $\alpha = 0$.

A limitation of the linear filter (1.5) is that it applies the same amount of regularization throughout the domain. This may over-regularize laminar or well-resolved regions and remove physically relevant structures. To address this issue, a nonlinear spatially adaptive filter was introduced in [29]:

$$-\alpha^2\nabla\cdot\big(a(\boldsymbol{v},q,\boldsymbol{f})\nabla\overline{\boldsymbol{v}}\big)+\overline{\boldsymbol{v}}+\nabla\lambda=\boldsymbol{v},\quad \nabla\cdot\overline{\boldsymbol{v}}=0\quad\text{in}\quad\Omega,\qquad \overline{\boldsymbol{v}}=\boldsymbol{v}\quad\text{on}\quad\partial\Omega. \tag{1.6}$$

The indicator function $0\le a(\boldsymbol{u},p,\boldsymbol{f})\le 1$ controls the location where filtering is applied. Several choices have been proposed in the literature [21,22,29].

The divergence constraint in (1.6) leads to a mixed filter problem, which increases the computational cost. To avoid this additional saddle-point solve, an efficient nonlinear filter stabilization method was proposed in [40]:

$$-\alpha^2\nabla\cdot\big(a(\boldsymbol{v},q,\boldsymbol{f})\nabla\overline{\boldsymbol{v}}\big)+\overline{\boldsymbol{v}}-\Gamma\nabla\nabla\cdot\overline{\boldsymbol{v}}=\boldsymbol{v}-\chi\nabla\nabla\cdot\boldsymbol{v}\quad\text{in}\quad\Omega,\qquad \overline{\boldsymbol{v}}=\boldsymbol{v}\quad\text{on}\quad\partial\Omega. \tag{1.7}$$

Here Γ and χ are grad-div parameters, with $\Gamma>\chi$, that weakly control the divergence of the filtered velocity.

The Leray-α regularization has been used for Rayleigh-Bénard convection [1,41,42], demonstrating its effectiveness for buoyancy-driven flows. However, the application to bioconvection has not been considered.

1.3. Main contributions. Various numerical methods have been developed for bioconvective flows. Early computational studies focused on the formation and stability of gyrotactic plumes. In particular, Ghorai and Hill investigated the development of individual plumes and periodic plume arrays using conservative finite-difference schemes [18–20]. Spectral Galerkin approximations and their convergence rates were studied in [13]. Finite element approaches have also been developed for generalized bioconvective flows. In particular, [9] established well-posedness results, derived finite element error estimates, and simulated pattern formation, while [14] introduced a second-order partitioned method for time-dependent bioconvective flows. More recently, [12] developed an adaptive fully mixed finite element method for stationary generalized bioconvective flows. These works reproduce characteristic plume structures and examine the dependence of the dynamics on model parameters. However, regularization and spatially adaptive filtering techniques remain unexplored for geotactic bioconvection. Moreover, accurate long-time simulations may require fine spatial resolution and become computationally expensive.

To address these challenges, we make the following contributions.

(a) We develop a spatially adaptive Leray-α regularization framework for [40] the geotactic bioconvection. The regularized model preserves key structural properties of the original system, including conservation of the total microorganism mass and the kinetic–potential energy balance.

(b) We design an energy-stable finite element method for the regularized model. The method solves the filter problem, the Navier-Stokes equations, and the transport problem in a partitioned way through a subiteration procedure. We prove stability of the semi-discrete scheme and establish convergence of the decoupled subiteration.

(c) We analyze the discrepancy between the grad-div filter (1.7) and the classical Stokes-type adaptive filter (1.6) at both the continuous and discrete levels. At the continuous level, increasing the grad-div parameter Γ improves the approximation to the Stokes-type filter. At the discrete level, however, we identify a competing effect driven by discrete divergence residuals, which limits the benefit of taking Γ and χ arbitrarily large. This analysis informs the selection of a suitable parameter range.

(d) We present numerical experiments for geotactic bioconvection, including both constant-viscosity and concentration-dependent viscosity cases. In both settings, the filtered method on coarse meshes captures the dominant large-scale dynamics obtained by the standard finite element method on much finer meshes, while substantially reducing computational cost.

2. The spatially adaptive Leray-α bioconvection model. In this section, we introduce an adaptive filtered formulation of the bioconvection system (1.1). The key idea is to replace the advecting velocity in the momentum convection term by a spatially filtered counterpart $\overline{\boldsymbol{u}}$, obtained via an adaptive Helmholtz filter. This smooths the small-scale features of the advecting field while preserving the large-scale dynamics, enabling accurate simulations on coarser meshes. We suppress the arguments $(\boldsymbol{x},t)$ when no ambiguity arises.

The filtered bioconvection system reads:

$$\begin{aligned}
&\frac{\partial \boldsymbol{u}}{\partial t} - \nabla\cdot\big(\nu(c)D(\boldsymbol{u})\big) + (\overline{\boldsymbol{u}}\cdot\nabla)\boldsymbol{u} + \frac{1}{2}(\nabla\cdot\overline{\boldsymbol{u}})\boldsymbol{u} = -\nabla p - g\big(1+\gamma c\big)\boldsymbol{i}_d + \boldsymbol{f},\\
&\nabla\cdot\boldsymbol{u} = 0,\\
&\frac{\partial c}{\partial t} - \Theta\Delta c + (\boldsymbol{u}\cdot\nabla)c + U\frac{\partial c}{\partial x_d} = 0.
\end{aligned} \tag{2.1}$$

The boundary conditions remain the same as those for the unfiltered system (1.2). The filtered velocity $\overline{\boldsymbol{u}}$ is defined as the solution of adaptive Helmholtz filter with grad-div stabilization [40]:

$$-\alpha^2\nabla\cdot\big(a(\boldsymbol{u})\nabla\overline{\boldsymbol{u}}\big) + \overline{\boldsymbol{u}} - \Gamma\nabla\nabla\cdot\overline{\boldsymbol{u}} = \boldsymbol{u} - \chi\nabla\nabla\cdot\boldsymbol{u} \quad \text{in} \quad \Omega, \qquad \overline{\boldsymbol{u}} = \boldsymbol{u} \quad \text{on} \quad \partial\Omega. \tag{2.2}$$

REMARK 1. *The additional term $(\nabla\cdot\overline{\boldsymbol{u}})\boldsymbol{u}/2$ in the momentum equation is included so that the filtered convection operator is skew-symmetric. This term vanishes if $\overline{\boldsymbol{u}}$ is pointwise divergence-free. However, the grad-div filter (2.2) does not impose the exact incompressibility constraint $\nabla\cdot\overline{\boldsymbol{u}} = 0$, but rather penalizes the divergence of the filtered velocity. For this reason, we retain the skew-symmetric convection form. By Lemma 3.3, the resulting convective operator does not contribute to the kinetic-energy balance under the homogeneous Dirichlet boundary condition.*

REMARK 2. *The filter radius $\alpha \geq 0$ controls the degree of spatial regularization. The unfiltered system (1.1) is recovered when $\alpha = 0$. The grad-div parameters Γ and χ, with $\Gamma > \chi$, weakly control the divergence of the filtered velocity. In Section 6, we analyze the effect of these parameters.*

We next observe that the regularized model (2.1) preserves key structural properties of the original system (1.1). Since the concentration equation and its boundary condition are unchanged, the total microorganism mass remains conserved. Furthermore, the total energy balance is unchanged. Testing the momentum equation with $\boldsymbol{u}$ and using Lemma 3.3, we obtain

$$\frac{d}{dt}\mathrm{KE}(t) + \int_\Omega \nu(c)|D(\boldsymbol{u})|^2\,d\boldsymbol{x} = -\gamma g\int_\Omega c u_d\,d\boldsymbol{x} + \int_\Omega \boldsymbol{f}\cdot\boldsymbol{u}\,d\boldsymbol{x},$$

where the constant gravity term vanishes under the incompressibility and homogeneous Dirichlet boundary conditions. On the other hand, testing the concentration equation with $\gamma g(x_d - x_d^{\min})$

$$\frac{d}{dt}\mathrm{PE}(t) = \gamma g\int_\Omega c u_d\,d\boldsymbol{x} - \gamma g\Theta\int_\Omega \frac{\partial c}{\partial x_d}\,d\boldsymbol{x} + \gamma g U M_0.$$

Adding the two identities yields

$$\frac{d}{dt}\big(\mathrm{KE}(t)+\mathrm{PE}(t)\big) + \int_\Omega \nu(c)|D(\boldsymbol{u})|^2\,d\boldsymbol{x} = -\gamma g\Theta\int_\Omega \frac{\partial c}{\partial x_d}\,d\boldsymbol{x} + \gamma g U M_0 + \int_\Omega \boldsymbol{f}\cdot\boldsymbol{u}\,d\boldsymbol{x},$$

which is the same total energy balance as (1.3).

3. Notation and preliminaries. In this section, we collect the notation, assumptions, and standard analytical tools. Throughout the paper, the $L^2(\Omega)$ inner product and norm are denoted by $(\cdot,\cdot)_\Omega$ and $\|\cdot\|$, respectively. All other norms will be clearly labeled. We consider wall-bounded flows and use the following function spaces:

$$\boldsymbol{V} = [H_0^1(\Omega)]^d = \{\boldsymbol{v}\in[H^1(\Omega)]^d,\ \boldsymbol{v} = 0 \ \text{ on } \partial\Omega\}, \quad Q = L_0^2(\Omega) = \{q\in L^2(\Omega),\ \int_\Omega q = 0\}, \quad S = H^1(\Omega).$$

Here $\boldsymbol{V}$, Q, and S denote the velocity, pressure, and concentration spaces, respectively.

We make the following assumptions on the viscosity and the indicator function.

ASSUMPTION 1 (Viscosity). *The kinematic viscosity $\nu:\mathbb{R}\to\mathbb{R}$ is Lipschitz continuous. Moreover, there exist positive constants ν_*, ν^*, and L_ν such that*

$$\nu_* \leq \nu(c) \leq \nu^*, \qquad |\nu(c_1)-\nu(c_2)| \leq L_\nu|c_1-c_2|, \qquad \forall c, c_1, c_2\in\mathbb{R}.$$

This assumption is justified by applications [3,26,34], where the lower bound ν_* represents the viscosity of the culture fluid in the absence of microorganisms. The upper bound ν^* is physically reasonable because the volume fraction of microorganisms is bounded by the finite size and packing structure of the cells [19].

ASSUMPTION 2 (Indicator function). *The indicator function $a : \mathbb{R}^d \to \mathbb{R}$ is Lipschitz continuous. Moreover, there exist positive constants $a_{\min}$ and L_a such that*

$$0 < a_{\min} \le a(\boldsymbol{u}) \le 1, \qquad |a(\boldsymbol{u}_1) - a(\boldsymbol{u}_2)| \le L_a|\boldsymbol{u}_1 - \boldsymbol{u}_2|, \qquad \forall\, \boldsymbol{u}, \boldsymbol{u}_1, \boldsymbol{u}_2 \in \mathbb{R}^d.$$

REMARK 3. *The lower bound $a_{\min} > 0$ ensures coercivity of the adaptive filter. In computations, the indicator function is chosen to be small in well-resolved regions and close to one in under-resolved regions [29]. Specific choices of $a(\cdot)$ will be given in Section 7.*

The following identities are used in the time-discrete analysis.

LEMMA 3.1 (Polarization identity). *For $\theta_n \in [0,1]$ and $\phi_{n+\theta_n} = \theta_n\phi_{n+1} + (1-\theta_n)\phi_n$,*

$$(\phi_{n+1} - \phi_n, \phi_{n+\theta_n})_\Omega = \frac{1}{2}(\|\phi_{n+1}\|^2 - \|\phi_n\|^2) + (\theta_n - \frac{1}{2})\|\phi_{n+1} - \phi_n\|^2.$$

LEMMA 3.2 (Convexity bound). *For $\theta_n \in [0,1]$ and any $\phi_{n+1}, \phi_n \in L^2(\Omega)$:*

$$\|\phi_{n+\theta_n}\|^2 \le \theta_n\|\phi_{n+1}\|^2 + (1-\theta_n)\|\phi_n\|^2 \le \|\phi_{n+1}\|^2 + \|\phi_n\|^2.$$

LEMMA 3.3 (Skew-symmetry of the convection operator). *Let $\boldsymbol{w} \in [H^1(\Omega)]^d$ and $\boldsymbol{v} \in [H_0^1(\Omega)]^d$. Then*

$$\big((\boldsymbol{w}\cdot\nabla)\boldsymbol{v}, \boldsymbol{v}\big)_\Omega + \frac{1}{2}\big((\nabla\cdot\boldsymbol{w})\boldsymbol{v}, \boldsymbol{v}\big)_\Omega = 0.$$

Proof. Using integration by parts and $\boldsymbol{v} = 0$ on $\partial\Omega$,

$$\big((\boldsymbol{w}\cdot\nabla)\boldsymbol{v}, \boldsymbol{v}\big)_\Omega = \frac{1}{2}(\boldsymbol{w}, \nabla|\boldsymbol{v}|^2)_\Omega = -\frac{1}{2}\big((\nabla\cdot\boldsymbol{w})\boldsymbol{v}, \boldsymbol{v}\big)_\Omega.$$

□

We finally collect the standard inequalities.

LEMMA 3.4 (Korn–Poincaré inequality [28]). *There exists $C_K > 0$ depending only on Ω such that for all $\boldsymbol{u} \in H_0^1(\Omega)^d$:*

$$\|\boldsymbol{u}\| \le \|\boldsymbol{u}\|_{H^1(\Omega)} \le C_K\|D(\boldsymbol{u})\|.$$

LEMMA 3.5 (Gagliardo–Nirenberg (Ladyzhenskaya) inequality [27]). *There exists $C_L > 0$ depending only on Ω ($d = 2$) such that for all $\varphi \in H_0^1(\Omega)$, $\psi \in H^1(\Omega)$:*

$$\|\varphi\|_{L^4}^2 \le C_L\,\|\varphi\|\,\|\nabla\varphi\|, \qquad \|\psi\|_{L^4}^2 \le C_L\,\|\psi\|\|\psi\|_{H^1(\Omega)}.$$

LEMMA 3.6 (Discrete Grönwall inequality [23]). *Let $\{a_n\}_{n=0}^N$, $\{b_n\}_{n=0}^{N-1}$, $\{g_n\}_{n=0}^{N-1}$ and $\{\tau_n\}_{n=0}^{N-1}$ be non-negative sequences. Suppose*

$$a_N \le a_0 + \sum_{n=0}^{N-1}\tau_n b_n a_n + \sum_{n=0}^{N-1}\tau_n g_n,$$

Then

$$a_N \le \exp\left(\sum_{n=0}^{N-1}\tau_n b_n\right)\left[a_0 + \sum_{n=0}^{N-1}\tau_n g_n\right].$$

4. Time discretization and the decoupled algorithm. In this section, we describe the time discretization of the filtered bioconvection system (2.1)–(2.2) and the decoupled algorithm used to solve the resulting nonlinear system. Let $\{t_n\}_{0\le n\le N}$ be a partition of $[0,T]$ with time steps $\tau_n = t_{n+1} - t_n$. We also denote $t_{n+\theta_n} = t_n + \theta_n\tau_n$, for any $\theta_n \in [0.5,1]$. The time discretization is based on a refactorized one-legged θ-method [10], and the nonlinear system at each time step is solved using an Oseen-type decoupled subiteration [28]. For clarity, we first summarize the complete solution procedure and then describe each component in detail.

Algorithm 1 Adaptive filtered solver for the bioconvection system

1: **Given:** initial data $(\boldsymbol{u}_0, c_0)$, time step $\{\tau_n\}$, lag parameters $\{\theta_n\}$, final time T, filter parameters α, Γ, χ, tolerance tol, and maximum number of subiterations $\kappa_{\max}$.
2: **for** $n = 0,1,2,\ldots,N-1$, where $\sum_n \tau_n = T$ **do**
3: **Initialize subiteration:** $\boldsymbol{u}_{n+\theta_n}^{(0)} = \overline{\boldsymbol{u}}_{n+\theta_n}^{(0)} = (1+\theta_n)\boldsymbol{u}_n - \theta_n\boldsymbol{u}_{n-1}$, $\quad c_{n+\theta_n}^{(0)} = (1+\theta_n)c_n - \theta_n c_{n-1}$.
4: **for** $\kappa = 0,1,\ldots,\kappa_{\max}-1$ **do**
5: Solve the **Helmholtz filter** problem (7.2) for $\overline{\boldsymbol{u}}_H^{(\kappa+1)}$.
6: Compute the **indicator function** $a(\boldsymbol{u})$ using (7.1).
7: Solve the **adaptive Helmholtz filter** for $\overline{\boldsymbol{u}}_{n+\theta_n}^{(\kappa+1)}$.
8: Solve the linearized **Navier–Stokes** problem for $\boldsymbol{u}_{n+\theta_n}^{(\kappa+1)}$.
9: Solve the **concentration transport** problem for $c_{n+\theta_n}^{(\kappa+1)}$.
10: **if** the relative change in $\left(\boldsymbol{u}_{n+\theta_n}^{(\kappa+1)}, c_{n+\theta_n}^{(\kappa+1)}\right)$ is less than tol **then**
11: Set $\boldsymbol{u}_{n+\theta_n} = \boldsymbol{u}_{n+\theta_n}^{(\kappa+1)}$, $\quad c_{n+\theta_n} = c_{n+\theta_n}^{(\kappa+1)}$, and terminate the subiteration.
12: **end if**
13: **end for**
14: **Extrapolate:** $\boldsymbol{u}_{n+1} = \frac{1}{\theta_n}\boldsymbol{u}_{n+\theta_n} - \left(\frac{1}{\theta_n} - 1\right)\boldsymbol{u}_n$, $\quad c_{n+1} = \frac{1}{\theta_n}c_{n+\theta_n} - \left(\frac{1}{\theta_n} - 1\right)c_n$.
15: **end for**

Steps 7, 8, and 9 describe the decoupled filter, momentum, and concentration equations. They are detailed below as follows.

Step 7: find $\overline{\boldsymbol{u}}_{n+\theta_n}^{(\kappa+1)} \in \boldsymbol{V}$ such that

$$\overline{\boldsymbol{u}}_{n+\theta_n}^{(\kappa+1)} - \alpha^2\nabla\cdot\left(a(\boldsymbol{u}_{n+\theta_n}^{(\kappa)})\nabla\overline{\boldsymbol{u}}_{n+\theta_n}^{(\kappa+1)}\right) - \Gamma\nabla\nabla\cdot\overline{\boldsymbol{u}}_{n+\theta_n}^{(\kappa+1)} = \boldsymbol{u}_{n+\theta_n}^{(\kappa)} - \chi\nabla\nabla\cdot\boldsymbol{u}_{n+\theta_n}^{(\kappa)} \qquad \text{in } \Omega. \tag{4.1}$$

Step 8: find $(\boldsymbol{u}_{n+\theta_n}^{(\kappa+1)}, p_{n+\theta_n}^{(\kappa+1)}) \in \boldsymbol{V}\times Q$ such that

$$\begin{aligned}\frac{\boldsymbol{u}_{n+\theta_n}^{(\kappa+1)} - \boldsymbol{u}_n}{\theta_n\tau_n} - \nabla\cdot(\nu(c_{n+\theta_n}^{(\kappa)})D(\boldsymbol{u}_{n+\theta_n}^{(\kappa+1)})) + (\overline{\boldsymbol{u}}_{n+\theta_n}^{(\kappa)}\cdot\nabla)\boldsymbol{u}_{n+\theta_n}^{(\kappa+1)} + \frac{1}{2}(\nabla\cdot\overline{\boldsymbol{u}}_{n+\theta_n}^{(\kappa)})\boldsymbol{u}_{n+\theta_n}^{(\kappa+1)} \\ = -\nabla p_{n+\theta_n}^{(\kappa+1)} - g(1+\gamma c_{n+\theta_n}^{(\kappa)})\boldsymbol{i}_d + \boldsymbol{f}_{n+\theta_n} \qquad \text{in } \Omega \\ \nabla\cdot\boldsymbol{u}_{n+\theta_n}^{(\kappa+1)} = 0 \qquad \text{in } \Omega.\end{aligned} \tag{4.2}$$

Step 9: find $c_{n+\theta_n}^{(\kappa+1)} \in S$ such that

$$\frac{c_{n+\theta_n}^{(\kappa+1)} - c_n}{\theta_n\tau_n} - \Theta\Delta c_{n+\theta_n}^{(\kappa+1)} + (\boldsymbol{u}_{n+\theta_n}^{(\kappa)}\cdot\nabla)c_{n+\theta_n}^{(\kappa+1)} + U\frac{\partial c_{n+\theta_n}^{(\kappa+1)}}{\partial x_d} = 0 \qquad \text{in } \Omega. \tag{4.3}$$

Because all coupling terms are lagged from the previous subiteration, the filter, momentum, and concentration solves at subiteration $\kappa+1$ are mutually independent and can be performed concurrently. In Section 5.1, we show that, as $\kappa\to\infty$, the sequences of iterates converge linearly,

$$\boldsymbol{u}_{n+\theta_n}^{(\kappa)} \longrightarrow \boldsymbol{u}_{n+\theta_n}, \qquad c_{n+\theta_n}^{(\kappa)} \longrightarrow c_{n+\theta_n},$$

to the solution of

$$\begin{aligned}
&\overline{\boldsymbol{u}}_{n+\theta_n} - \alpha^2 \nabla \cdot \Big(a(\boldsymbol{u}_{n+\theta_n}) \nabla \overline{\boldsymbol{u}}_{n+\theta_n} \Big) - \Gamma \nabla \nabla \cdot \overline{\boldsymbol{u}}_{n+\theta_n} = \boldsymbol{u}_{n+\theta_n} - \chi \nabla \nabla \cdot \boldsymbol{u}_{n+\theta_n}, \\
&\frac{\boldsymbol{u}_{n+\theta_n} - \boldsymbol{u}_n}{\theta_n \tau_n} - \nabla \cdot \big(\nu(c_{n+\theta_n}) D(\boldsymbol{u}_{n+\theta_n}) \big) + (\overline{\boldsymbol{u}}_{n+\theta_n} \cdot \nabla) \boldsymbol{u}_{n+\theta_n} + \frac{1}{2} (\nabla \cdot \overline{\boldsymbol{u}}_{n+\theta_n}) \boldsymbol{u}_{n+\theta_n} \\
&\qquad\qquad = -\nabla p_{n+\theta_n} - g(1 + \gamma c_{n+\theta_n}) \boldsymbol{i}_d + \boldsymbol{f}_{n+\theta_n}, \\
&\nabla \cdot \boldsymbol{u}_{n+\theta_n} = 0, \\
&\frac{c_{n+\theta_n} - c_n}{\theta_n \tau_n} - \Theta \Delta c_{n+\theta_n} + \big(\boldsymbol{u}_{n+\theta_n} \cdot \nabla \big) c_{n+\theta_n} + U \frac{\partial c_{n+\theta_n}}{\partial x_d} = 0.
\end{aligned} \tag{4.4}$$

The purpose of the extrapolation in Step 14 is to increase the accuracy. In particular, when $\theta = \frac{1}{2}$, the converged system (4.4) combined with extrapolation corresponds to the midpoint method, which is second-order accurate [8]. As the extrapolation is only performed for the time-dependent variables, it is not applied to the filtered velocity. In particular, the converged and extrapolated system can be written as the following one-legged θ-method:

$$\begin{aligned}
&\overline{\boldsymbol{u}}_{n+\theta_n} - \alpha^2 \nabla \cdot \Big(a(\boldsymbol{u}_{n+\theta_n}) \nabla \overline{\boldsymbol{u}}_{n+\theta_n} \Big) - \Gamma \nabla \nabla \cdot \overline{\boldsymbol{u}}_{n+\theta_n} = \boldsymbol{u}_{n+\theta_n} - \chi \nabla \nabla \cdot \boldsymbol{u}_{n+\theta_n}, \\
&\frac{\boldsymbol{u}_{n+1} - \boldsymbol{u}_n}{\tau_n} - \nabla \cdot \big(\nu(c_{n+\theta_n}) D(\boldsymbol{u}_{n+\theta_n}) \big) + (\overline{\boldsymbol{u}}_{n+\theta_n} \cdot \nabla) \boldsymbol{u}_{n+\theta_n} + \frac{1}{2} (\nabla \cdot \overline{\boldsymbol{u}}_{n+\theta_n}) \boldsymbol{u}_{n+\theta_n} \\
&\qquad\qquad = -\nabla p_{n+\theta_n} - g(1 + \gamma c_{n+\theta_n}) \boldsymbol{i}_d + \boldsymbol{f}_{n+\theta_n}, \\
&\nabla \cdot \boldsymbol{u}_{n+1} = 0, \\
&\frac{c_{n+1} - c_n}{\tau_n} - \Theta \Delta c_{n+\theta_n} + \big(\boldsymbol{u}_{n+\theta_n} \cdot \nabla \big) c_{n+\theta_n} + U \frac{\partial c_{n+\theta_n}}{\partial x_d} = 0.
\end{aligned} \tag{4.5}$$

5. Analysis of the semi-discrete scheme. In this section, we analyze Algorithm 1. We first establish conservation of total microorganism mass. We then prove that the decoupled subiteration (4.1)–(4.3) converges linearly to the solution of the coupled nonlinear system (4.4) at each time step. Finally, we establish a stability estimate for the extrapolated time-discrete problem (4.5).

PROPOSITION 5.1 (Semi-discrete mass conservation). *The semi-discrete concentration equation in* (4.5) *preserves the total microorganism mass:*

$$\int_\Omega c_{n+1} \, d\boldsymbol{x} = \int_\Omega c_n \, d\boldsymbol{x}, \qquad n = 0, \ldots, N-1.$$

Consequently,

$$\int_\Omega c_n \, d\boldsymbol{x} = \int_\Omega c_0 \, d\boldsymbol{x} =: M_0, \qquad n = 0, \ldots, N.$$

Proof. Integrating the concentration equation in (4.5) over Ω and using the divergence theorem gives

$$\frac{1}{\tau_n} \left(\int_\Omega c_{n+1} \, d\boldsymbol{x} - \int_\Omega c_n \, d\boldsymbol{x} \right) - \int_{\partial\Omega} \left(\Theta \frac{\partial c_{n+\theta_n}}{\partial \boldsymbol{n}} - U c_{n+\theta_n} n_d \right) ds = 0,$$

where the fluid convection term vanishes because

$$\nabla \cdot \boldsymbol{u}_{n+\theta_n} = 0, \qquad \boldsymbol{u}_{n+\theta_n} = 0 \quad \text{on } \partial\Omega.$$

The boundary integral vanishes by the no-flux boundary condition (1.2), which gives the desired result. □

5.1. Convergence of the subiteration. In this subsection, we prove that the decoupled subiteration (4.1)–(4.3) converges linearly to the solution of the coupled system (4.4) at each time step. Throughout this subsection, the time level n is fixed. We define the subiteration errors

$$\boldsymbol{\delta}_{\overline{\boldsymbol{u}}}^{(\kappa)} = \overline{\boldsymbol{u}}_{n+\theta_n} - \overline{\boldsymbol{u}}_{n+\theta_n}^{(\kappa)}, \qquad \boldsymbol{\delta}_{\boldsymbol{u}}^{(\kappa)} = \boldsymbol{u}_{n+\theta_n} - \boldsymbol{u}_{n+\theta_n}^{(\kappa)}, \qquad \delta_p^{(\kappa)} = p_{n+\theta_n} - p_{n+\theta_n}^{(\kappa)}, \qquad \delta_c^{(\kappa)} = c_{n+\theta_n} - c_{n+\theta_n}^{(\kappa)}.$$

All constants in this subsection are independent of the subiteration index κ. We define the combined subiteration energy

$$\mathscr{E}^{(\kappa)} = \|\delta_{\boldsymbol{u}}^{(\kappa)}\|^2 + \|\delta_c^{(\kappa)}\|^2 + \frac{1}{2}\|\delta_{\overline{\boldsymbol{u}}}^{(\kappa)}\|^2 + \frac{\alpha^2 a_{\min}}{2}\|\nabla\delta_{\overline{\boldsymbol{u}}}^{(\kappa)}\|^2 + \frac{\nu_*}{8}\|D(\delta_{\boldsymbol{u}}^{(\kappa)})\|^2 + \frac{\Theta}{4}\|\nabla\delta_c^{(\kappa)}\|^2. \tag{5.1}$$

THEOREM 5.2 (Linear convergence of the subiteration). *Let $d = 2$. Under Assumptions 1 and 2, suppose that the coupled system (4.4) admits a solution $(\boldsymbol{u}_{n+\theta_n}, \overline{\boldsymbol{u}}_{n+\theta_n}, c_{n+\theta_n}) \in [H^2(\Omega)]^d \times [H^1(\Omega)]^d \times H^1(\Omega)$, and that the time step satisfies*

$$\theta_n\tau_n < \frac{1}{2\max(C_\ell, C_r)}. \tag{5.2}$$

Then, there exist constants $C_\ell, C_r > 0$, independent of κ and depending only on the physical parameters, filter parameters, domain constants, and norms of the converged solution, such that the subiteration error satisfies

$$\mathscr{E}^{(\kappa+1)} \le \rho\,\mathscr{E}^{(\kappa)}, \qquad \text{where } \rho = \frac{C_\ell}{1/(\theta_n\tau_n) - C_r} < 1. \tag{5.3}$$

Proof. The proof proceeds in five steps.

Step 1: Error equations. We begin by subtracting the subiteration equations (4.1)–(4.3) from the coupled system (4.4). For the filter equation, after adding and subtracting $\alpha^2\nabla\cdot\left(a(\boldsymbol{u}_{n+\theta_n}^{(\kappa)})\nabla\overline{\boldsymbol{u}}_{n+\theta_n}\right)$, we obtain

$$\begin{aligned}
&\delta_{\overline{\boldsymbol{u}}}^{(\kappa+1)} - \alpha^2\nabla\cdot\left(a(\boldsymbol{u}_{n+\theta_n}^{(\kappa)})\nabla\delta_{\overline{\boldsymbol{u}}}^{(\kappa+1)}\right) - \Gamma\nabla\nabla\cdot\delta_{\overline{\boldsymbol{u}}}^{(\kappa+1)} \\
&\quad = \delta_{\boldsymbol{u}}^{(\kappa)} - \chi\nabla\nabla\cdot\delta_{\boldsymbol{u}}^{(\kappa)} + \alpha^2\nabla\cdot\left(\left[a(\boldsymbol{u}_{n+\theta_n}) - a(\boldsymbol{u}_{n+\theta_n}^{(\kappa)})\right]\nabla\overline{\boldsymbol{u}}_{n+\theta_n}\right).
\end{aligned} \tag{5.4}$$

For the momentum equation, after adding and subtracting the lagged viscosity and convection terms, we have

$$\begin{aligned}
&\frac{\delta_{\boldsymbol{u}}^{(\kappa+1)}}{\theta_n\tau_n} - \nabla\cdot\left(\nu(c_{n+\theta_n}^{(\kappa)})D(\delta_{\boldsymbol{u}}^{(\kappa+1)})\right) + \nabla\delta_p^{(\kappa+1)} + (\overline{\boldsymbol{u}}_{n+\theta_n}^{(\kappa)}\cdot\nabla)\delta_{\boldsymbol{u}}^{(\kappa+1)} + \frac{1}{2}(\nabla\cdot\overline{\boldsymbol{u}}_{n+\theta_n}^{(\kappa)})\delta_{\boldsymbol{u}}^{(\kappa+1)} \\
&\quad = -g\gamma\delta_c^{(\kappa)}\boldsymbol{i}_d + \nabla\cdot\left([\nu(c_{n+\theta_n}) - \nu(c_{n+\theta_n}^{(\kappa)})]D(\boldsymbol{u}_{n+\theta_n})\right) - (\delta_{\overline{\boldsymbol{u}}}^{(\kappa)}\cdot\nabla)\boldsymbol{u}_{n+\theta_n} - \frac{1}{2}(\nabla\cdot\delta_{\overline{\boldsymbol{u}}}^{(\kappa)})\boldsymbol{u}_{n+\theta_n},
\end{aligned} \tag{5.5}$$

with

$$\nabla\cdot\delta_{\boldsymbol{u}}^{(\kappa+1)} = 0. \tag{5.6}$$

For the concentration equation, after adding and subtracting $\boldsymbol{u}_{n+\theta_n}^{(\kappa)}\cdot\nabla c_{n+\theta_n}$, we obtain

$$\frac{\delta_c^{(\kappa+1)}}{\theta_n\tau_n} - \Theta\Delta\delta_c^{(\kappa+1)} + \boldsymbol{u}_{n+\theta_n}^{(\kappa)}\cdot\nabla\delta_c^{(\kappa+1)} + U\frac{\partial\delta_c^{(\kappa+1)}}{\partial x_d} = -\delta_{\boldsymbol{u}}^{(\kappa)}\cdot\nabla c_{n+\theta_n}. \tag{5.7}$$

Step 2: Filter error estimate. Testing (5.4) with $\delta_{\overline{\boldsymbol{u}}}^{(\kappa+1)}$, integrating by parts, and using (5.6), gives

$$\begin{aligned}
&\|\delta_{\overline{\boldsymbol{u}}}^{(\kappa+1)}\|^2 + \alpha^2\int_\Omega a(\boldsymbol{u}_{n+\theta_n}^{(\kappa)})|\nabla\delta_{\overline{\boldsymbol{u}}}^{(\kappa+1)}|^2\,d\boldsymbol{x} + \Gamma\|\nabla\cdot\delta_{\overline{\boldsymbol{u}}}^{(\kappa+1)}\|^2 \\
&\le \|\delta_{\boldsymbol{u}}^{(\kappa)}\|\|\delta_{\overline{\boldsymbol{u}}}^{(\kappa+1)}\| + \alpha^2\left|\int_\Omega\left[a(\boldsymbol{u}_{n+\theta_n}) - a(\boldsymbol{u}_{n+\theta_n}^{(\kappa)})\right]\nabla\overline{\boldsymbol{u}}_{n+\theta_n}\cdot\nabla\delta_{\overline{\boldsymbol{u}}}^{(\kappa+1)}\,d\boldsymbol{x}\right|.
\end{aligned}$$

By Assumption 2, Hölder's inequality, and Lemma 3.5,

$$\begin{aligned}
\alpha^2\left|\int_\Omega\left[a(\boldsymbol{u}_{n+\theta_n}) - a(\boldsymbol{u}_{n+\theta_n}^{(\kappa)})\right]\nabla\overline{\boldsymbol{u}}_{n+\theta_n}\cdot\nabla\delta_{\overline{\boldsymbol{u}}}^{(\kappa+1)}\,d\boldsymbol{x}\right| &\le \alpha^2 L_a\|\delta_{\boldsymbol{u}}^{(\kappa)}\|_{L^4}\|\nabla\overline{\boldsymbol{u}}_{n+\theta_n}\|_{L^4}\|\nabla\delta_{\overline{\boldsymbol{u}}}^{(\kappa+1)}\| \\
&\le C\alpha^2\|\nabla\overline{\boldsymbol{u}}_{n+\theta_n}\|_{L^4}\|\delta_{\boldsymbol{u}}^{(\kappa)}\|^{1/2}\|\nabla\delta_{\boldsymbol{u}}^{(\kappa)}\|^{1/2}\|\nabla\delta_{\overline{\boldsymbol{u}}}^{(\kappa+1)}\|.
\end{aligned}$$

Using Young's inequality and Lemma 3.4, we obtain

$$\frac{1}{2}\|\delta_{\overline{u}}^{(\kappa+1)}\|^2+\frac{\alpha^2}{2}a_{\min}\|\nabla\delta_{\overline{u}}^{(\kappa+1)}\|^2+\Gamma\|\nabla\cdot\delta_{\overline{u}}^{(\kappa+1)}\|^2\le\frac{\nu_*}{16}\|D(\delta_{\boldsymbol{u}}^{(\kappa)})\|^2+\big(C\|\nabla\overline{\boldsymbol{u}}_{n+\theta_n}\|_{L^4}^4+\frac{1}{2}\big)\,\|\delta_{\boldsymbol{u}}^{(\kappa)}\|^2,\quad(5.8)$$

where C depends only on L_a, C_L, C_K, α, ν_*, and $a_{\min}$.

Step 3: Momentum error estimate. Testing (5.5) with $\delta_{\boldsymbol{u}}^{(\kappa+1)}$, the pressure term vanishes by (5.6). The skew-symmetric convection block also vanishes by Lemma 3.3. Using $\nu(c)\ge\nu_*$, we get

$$\begin{aligned}\frac{1}{\theta_n\tau_n}\|\delta_{\boldsymbol{u}}^{(\kappa+1)}\|^2+\nu_*\|D(\delta_{\boldsymbol{u}}^{(\kappa+1)})\|^2&\le g\gamma\|\delta_c^{(\kappa)}\|\|\delta_{\boldsymbol{u}}^{(\kappa+1)}\|+L_\nu\|\delta_c^{(\kappa)}\|_{L^4}\|D(\boldsymbol{u}_{n+\theta_n})\|_{L^4}\|D(\delta_{\boldsymbol{u}}^{(\kappa+1)})\|\\&\quad+\Big|\big((\delta_{\overline{\boldsymbol{u}}}^{(\kappa)}\cdot\nabla)\boldsymbol{u}_{n+\theta_n},\delta_{\boldsymbol{u}}^{(\kappa+1)}\big)_\Omega\Big|+\frac{1}{2}\Big|\big((\nabla\cdot\delta_{\overline{\boldsymbol{u}}}^{(\kappa)})\boldsymbol{u}_{n+\theta_n},\delta_{\boldsymbol{u}}^{(\kappa+1)}\big)_\Omega\Big|.\end{aligned}$$

Applying Young's inequality to the buoyancy term, we have

$$g\gamma\|\delta_c^{(\kappa)}\|\|\delta_{\boldsymbol{u}}^{(\kappa+1)}\|\le\frac{1}{2}g\gamma\|\delta_c^{(\kappa)}\|^2+\frac{1}{2}g\gamma\|\delta_{\boldsymbol{u}}^{(\kappa+1)}\|^2.$$

The viscosity mismatch is controlled by Assumption 1, Lemma 3.5, and Young's inequality:

$$L_\nu\|\delta_c^{(\kappa)}\|_{L^4}\|D(\boldsymbol{u}_{n+\theta_n})\|_{L^4}\|D(\delta_{\boldsymbol{u}}^{(\kappa+1)})\|\le\frac{\nu_*}{4}\|D(\delta_{\boldsymbol{u}}^{(\kappa+1)})\|^2+\frac{\Theta}{4}\|\nabla\delta_c^{(\kappa)}\|^2+C_\nu\|D(\boldsymbol{u}_{n+\theta_n})\|_{L^4}^4\|\delta_c^{(\kappa)}\|^2,$$

where C_ν depends on L_ν, C_L, ν_*, and Θ.

For the first convective perturbation, Hölder's inequality and Lemma 3.5 give

$$\begin{aligned}\Big|\big((\delta_{\overline{\boldsymbol{u}}}^{(\kappa)}\cdot\nabla)\boldsymbol{u}_{n+\theta_n},\delta_{\boldsymbol{u}}^{(\kappa+1)}\big)_\Omega\Big|&\le\|\delta_{\overline{\boldsymbol{u}}}^{(\kappa)}\|\|\nabla\boldsymbol{u}_{n+\theta_n}\|_{L^4}\|\delta_{\boldsymbol{u}}^{(\kappa+1)}\|_{L^4}\\&\le\frac{1}{4}\|\delta_{\overline{\boldsymbol{u}}}^{(\kappa)}\|^2+\frac{\nu_*}{4}\|D(\delta_{\boldsymbol{u}}^{(\kappa+1)})\|^2+C_{u,1}\|\nabla\boldsymbol{u}_{n+\theta_n}\|_{L^4}^4\|\delta_{\boldsymbol{u}}^{(\kappa+1)}\|^2,\end{aligned}$$

where $C_{u,1}$ depends on C_L, C_K, and ν_*.

For the divergence perturbation,

$$\begin{aligned}\frac{1}{2}\Big|\big((\nabla\cdot\delta_{\overline{\boldsymbol{u}}}^{(\kappa)})\boldsymbol{u}_{n+\theta_n},\delta_{\boldsymbol{u}}^{(\kappa+1)}\big)_\Omega\Big|&\le\frac{1}{2}\|\nabla\delta_{\overline{\boldsymbol{u}}}^{(\kappa)}\|\|\boldsymbol{u}_{n+\theta_n}\|_{L^4}\|\delta_{\boldsymbol{u}}^{(\kappa+1)}\|_{L^4}\\&\le\frac{\alpha^2}{4}a_{\min}\|\nabla\delta_{\overline{\boldsymbol{u}}}^{(\kappa)}\|^2+\frac{\nu_*}{4}\|D(\delta_{\boldsymbol{u}}^{(\kappa+1)})\|^2+C_{u,2}\|\boldsymbol{u}_{n+\theta_n}\|_{L^4}^4\|\delta_{\boldsymbol{u}}^{(\kappa+1)}\|^2,\end{aligned}$$

where $C_{u,2}$ depends on C_L, C_K, α, $a_{\min}$, and ν_*.

Therefore,

$$\begin{aligned}\frac{1}{\theta_n\tau_n}\|\delta_{\boldsymbol{u}}^{(\kappa+1)}\|^2+\frac{\nu_*}{4}\|D(\delta_{\boldsymbol{u}}^{(\kappa+1)})\|^2&\le\frac{1}{4}\|\delta_{\overline{\boldsymbol{u}}}^{(\kappa)}\|^2+\frac{\Theta}{4}\|\nabla\delta_c^{(\kappa)}\|^2+\frac{\alpha^2}{4}a_{\min}\|\nabla\delta_{\overline{\boldsymbol{u}}}^{(\kappa)}\|^2\\&\quad+\big(\frac{1}{2}g\gamma+C_\nu\|D(\boldsymbol{u}_{n+\theta_n})\|_{L^4}^4\big)\,\|\delta_c^{(\kappa)}\|^2\\&\quad+\big(\frac{1}{2}g\gamma+C_{u,1}\|\nabla\boldsymbol{u}_{n+\theta_n}\|_{L^4}^4+C_{u,2}\|\boldsymbol{u}_{n+\theta_n}\|_{L^4}^4\big)\,\|\delta_{\boldsymbol{u}}^{(\kappa+1)}\|^2.\end{aligned}\quad(5.9)$$

Step 4: Concentration error estimate. Testing (5.7) with $\delta_c^{(\kappa+1)}$, using (5.6), the boundary conditions (1.2), and integration by parts, yields

$$\frac{1}{\theta_n\tau_n}\|\delta_c^{(\kappa+1)}\|^2+\Theta\|\nabla\delta_c^{(\kappa+1)}\|^2\le\Big|(\delta_{\boldsymbol{u}}^{(\kappa)}\cdot\nabla c_{n+\theta_n},\delta_c^{(\kappa+1)})_\Omega\Big|+U\Big|(\nabla\delta_c^{(\kappa+1)}\cdot\boldsymbol{i}_d,\delta_c^{(\kappa+1)})_\Omega\Big|.$$

For the first term, Young's inequality, Hölder's inequality, Lemma 3.4, and Lemma 3.5 give

$$\begin{aligned}\left|(\delta_{\boldsymbol{u}}^{(\kappa)}\cdot\nabla c_{n+\theta_n},\,\delta_c^{(\kappa+1)})_\Omega\right| &\le \|\delta_{\boldsymbol{u}}^{(\kappa)}\|_{L^4}\|\nabla c_{n+\theta_n}\|\|\delta_c^{(\kappa+1)}\|_{L^4}\\ &\le C\|\nabla c_{n+\theta_n}\|\|\delta_{\boldsymbol{u}}^{(\kappa)}\|^{1/2}\|\nabla\delta_{\boldsymbol{u}}^{(\kappa)}\|^{1/2}\|\delta_c^{(\kappa+1)}\|^{1/2}\|\nabla\delta_c^{(\kappa+1)}\|^{1/2}\\ &\le \frac{\nu_*}{16}\|D(\delta_{\boldsymbol{u}}^{(\kappa)})\|^2+\frac{\Theta}{4}\|\nabla\delta_c^{(\kappa+1)}\|^2+C_{u,3}\|\delta_{\boldsymbol{u}}^{(\kappa)}\|^2+C_c\|\nabla c_{n+\theta_n}\|^4\|\delta_c^{(\kappa+1)}\|^2,\end{aligned}$$

where $C_{u,3}$ and C_c depend on C_L, C_K, Θ, and ν_*.

The swimming term is estimated by

$$U\left|(\nabla\delta_c^{(\kappa+1)}\cdot\boldsymbol{i}_d,\,\delta_c^{(\kappa+1)})_\Omega\right| \le \frac{\Theta}{4}\|\nabla\delta_c^{(\kappa+1)}\|^2+\frac{U^2}{\Theta}\|\delta_c^{(\kappa+1)}\|^2.$$

Consequently,

$$\frac{1}{\theta_n\tau_n}\|\delta_c^{(\kappa+1)}\|^2+\frac{\Theta}{2}\|\nabla\delta_c^{(\kappa+1)}\|^2 \le \frac{\nu_*}{16}\|D(\delta_{\boldsymbol{u}}^{(\kappa)})\|^2+C_{u,3}\|\delta_{\boldsymbol{u}}^{(\kappa)}\|^2+\Big(C_c\|\nabla c_{n+\theta_n}\|^4+\frac{U^2}{\Theta}\Big)\|\delta_c^{(\kappa+1)}\|^2. \tag{5.10}$$

Step 5: Closing the contraction estimate. Adding (5.8), (5.9), and (5.10):

$$\begin{aligned}&\frac{1}{\theta_n\tau_n}\|\delta_{\boldsymbol{u}}^{(\kappa+1)}\|^2+\frac{1}{\theta_n\tau_n}\|\delta_c^{(\kappa+1)}\|^2+\frac{1}{2}\|\delta_{\overline{\boldsymbol{u}}}^{(\kappa+1)}\|^2+\frac{\alpha^2}{2}a_{\min}\|\nabla\delta_{\overline{\boldsymbol{u}}}^{(\kappa+1)}\|^2\\ &\quad+\Gamma\|\nabla\cdot\delta_{\overline{\boldsymbol{u}}}^{(\kappa+1)}\|^2+\frac{\nu_*}{4}\|D(\delta_{\boldsymbol{u}}^{(\kappa+1)})\|^2+\frac{\Theta}{2}\|\nabla\delta_c^{(\kappa+1)}\|^2\\ &\le C_r\big(\|\delta_{\boldsymbol{u}}^{(\kappa+1)}\|^2+\|\delta_c^{(\kappa+1)}\|^2\big)+C_\ell^{(1)}\big(\|\delta_{\boldsymbol{u}}^{(\kappa)}\|^2+\|\delta_c^{(\kappa)}\|^2\big)\\ &\quad+\frac{1}{4}\|\delta_{\overline{\boldsymbol{u}}}^{(\kappa)}\|^2+\frac{\alpha^2}{4}a_{\min}\|\nabla\delta_{\overline{\boldsymbol{u}}}^{(\kappa)}\|^2+\frac{\nu_*}{8}\|D(\delta_{\boldsymbol{u}}^{(\kappa)})\|^2+\frac{\Theta}{4}\|\nabla\delta_c^{(\kappa)}\|^2,\end{aligned} \tag{5.11}$$

where

$$\begin{aligned}C_r &= \max\Big(\frac{1}{2}g\gamma+C_{u,1}\|\nabla\boldsymbol{u}_{n+\theta_n}\|_{L^4}^4+C_{u,2}\|\boldsymbol{u}_{n+\theta_n}\|_{L^4}^4,\,C_c\|\nabla c_{n+\theta_n}\|^4+\frac{U^2}{\Theta}\Big),\\ C_\ell^{(1)} &= \max\Big(C_{u,3}+C\|\nabla\overline{\boldsymbol{u}}_{n+\theta_n}\|_{L^4}^4+\frac{1}{2},\,\frac{1}{2}g\gamma+C_\nu\|D(\boldsymbol{u}_{n+\theta_n})\|_{L^4}^4\Big).\end{aligned}$$

Observe that the κ-level gradient terms on the right-hand side of (5.11) appear with coefficients that are exactly one half of the corresponding $(\kappa+1)$-level coefficients on the left-hand side. This is by design in the choice of Young's inequality parameters. Moving the C_r-terms to the left-hand side and using $1/\theta_n\tau_n - C_r \ge 1/2\theta_n\tau_n$ (valid under condition (5.2)), we obtain

$$\begin{aligned}&\frac{1}{2\theta_n\tau_n}\big(\|\delta_{\boldsymbol{u}}^{(\kappa+1)}\|^2+\|\delta_c^{(\kappa+1)}\|^2\big)+\frac{1}{2}\|\delta_{\overline{\boldsymbol{u}}}^{(\kappa+1)}\|^2+\frac{\alpha^2}{2}a_{\min}\|\nabla\delta_{\overline{\boldsymbol{u}}}^{(\kappa+1)}\|^2+\frac{\nu_*}{4}\|D(\delta_{\boldsymbol{u}}^{(\kappa+1)})\|^2+\frac{\Theta}{2}\|\nabla\delta_c^{(\kappa+1)}\|^2\\ &\le C_\ell^{(1)}\big(\|\delta_{\boldsymbol{u}}^{(\kappa)}\|^2+\|\delta_c^{(\kappa)}\|^2\big)+\frac{1}{4}\|\delta_{\overline{\boldsymbol{u}}}^{(\kappa)}\|^2+\frac{\alpha^2}{4}a_{\min}\|\nabla\delta_{\overline{\boldsymbol{u}}}^{(\kappa)}\|^2+\frac{\nu_*}{8}\|D(\delta_{\boldsymbol{u}}^{(\kappa)})\|^2+\frac{\Theta}{4}\|\nabla\delta_c^{(\kappa)}\|^2.\end{aligned} \tag{5.12}$$

In terms of the combined error (5.1), the left-hand side of (5.12) is bounded below by $\min\big(1/2\theta_n\tau_n,1\big)\,\mathscr{E}^{(\kappa+1)}$, while the right-hand side is bounded above by $\max\big(C_\ell^{(1)},1/2\big)\,\mathscr{E}^{(\kappa)}$. Therefore, setting $C_\ell=\max\big(C_\ell^{(1)},1/2\big)$:

$$\mathscr{E}^{(\kappa+1)} \le \frac{C_\ell}{\min\big(\frac{1}{2\theta_n\tau_n},1\big)}\,\mathscr{E}^{(\kappa)}. \tag{5.13}$$

For $\theta_n\tau_n<1/2$ (which is implied by (5.2)), $\min\big(1/2\theta_n\tau_n,1\big)=1$, and we need $C_\ell<1$ for contraction. In general, for $\theta_n\tau_n$ small, $1/2\theta_n\tau_n\gg 1$, and the contraction constant is

$$\rho=\frac{C_\ell}{1/2\theta_n\tau_n}=2\theta_n\tau_nC_\ell,$$

which satisfies $\rho < 1$ whenever $\theta_n \tau_n < 1/2C_\ell$. Combining with the requirement $\theta_n \tau_n < 1/2C_r$, condition (5.2) ensures both $\rho < 1$ and the absorption of the $(\kappa+1)$-level terms. □

REMARK 4. *The constants C_ℓ and C_r depend on norms of the converged solution such as $\|\nabla \boldsymbol{u}_{n+\theta_n}\|_{L^4}$, $\|D(\boldsymbol{u}_{n+\theta_n})\|_{L^4}$, $\|\boldsymbol{u}_{n+\theta_n}\|_{L^4}$, $\|\nabla \overline{\boldsymbol{u}}_{n+\theta_n}\|_{L^4}$, and $\|\nabla c_{n+\theta_n}\|$. In $d = 2$, the L^4 norms of the gradient are controlled by H^2 regularity via the Sobolev embedding $H^1(\Omega) \hookrightarrow L^4(\Omega)$. The concentration only requires $c_{n+\theta_n} \in H^1(\Omega)$ for the present analysis. The same argument extends to $d = 3$ using the corresponding Gagliardo–Nirenberg inequalities and stronger regularity assumptions.*

REMARK 5. *Since $\rho = O(\theta_n \tau_n)$, as $\tau_n \to 0$, smaller time steps yield faster convergence. In practice, very few subiterations (typically 2–3) suffice per time step.*

5.2. Stability of the semi-discrete scheme. In this subsection, we establish a stability of the semi-discrete system (4.5).

THEOREM 5.3 (Semi-discrete stability). *Under Assumptions 1, 2, suppose that $\theta_n \in [1/2, 1]$ and that the time step satisfies*

$$\tau_n M \le \frac{1}{2}, \quad \text{where} \quad M = g^2\gamma^2 \frac{C_K^2}{\nu_*} + \frac{U^2}{\Theta}. \tag{5.14}$$

Define the discrete energy $E_n = \|\boldsymbol{u}_n\|^2 + \|c_n\|^2$. Then, the numerical solution satisfies

$$\begin{aligned} &E_N + \sum_{n=0}^{N-1} (2\theta_n - 1)\big[\|\boldsymbol{u}_{n+1} - \boldsymbol{u}_n\|^2 + \|c_{n+1} - c_n\|^2\big] \\ &\quad + \sum_{n=0}^{N-1} 2\tau_n \int_\Omega \big(\nu(c_{n+\theta_n}) - \nu_*\big)|D(\boldsymbol{u}_{n+\theta_n})|^2\, d\boldsymbol{x} + \sum_{n=0}^{N-1} \tau_n \Theta \|\nabla c_{n+\theta_n}\|^2 \\ &\le E_0 + 2MT\, e^{4MT}\left(E_0 + \frac{2C_K^2}{\nu_*}\sum_{n=0}^{N-1}\tau_n \|\boldsymbol{f}_{n+\theta_n}\|^2\right) + \frac{C_K^2}{\nu_*}\sum_{n=0}^{N-1}\tau_n\|\boldsymbol{f}_{n+\theta_n}\|^2. \end{aligned} \tag{5.15}$$

Proof. The proof proceeds in four steps.

Step 1: Filter estimate. Testing the filter equation in (4.5) with $\overline{\boldsymbol{u}}_{n+\theta_n}$ and integrating by parts:

$$\|\overline{\boldsymbol{u}}_{n+\theta_n}\|^2 + \alpha^2 \int_\Omega a(\boldsymbol{u}_{n+\theta_n})\,|\nabla \overline{\boldsymbol{u}}_{n+\theta_n}|^2\, d\boldsymbol{x} + \Gamma\|\nabla\cdot\overline{\boldsymbol{u}}_{n+\theta_n}\|^2 = (\boldsymbol{u}_{n+\theta_n}, \overline{\boldsymbol{u}}_{n+\theta_n})_\Omega + \chi(\nabla\cdot\boldsymbol{u}_{n+\theta_n}, \nabla\cdot\overline{\boldsymbol{u}}_{n+\theta_n})_\Omega.$$

Since $\nabla\cdot\boldsymbol{u}_{n+\theta_n} = \theta_n \nabla\cdot\boldsymbol{u}_{n+1} + (1-\theta_n)\nabla\cdot\boldsymbol{u}_n = 0$, the χ-term vanishes. Applying Assumption 2 and Young's inequality:

$$\frac{1}{2}\|\overline{\boldsymbol{u}}_{n+\theta_n}\|^2 + \alpha^2 a_{\min}\|\nabla\overline{\boldsymbol{u}}_{n+\theta_n}\|^2 + \Gamma\|\nabla\cdot\overline{\boldsymbol{u}}_{n+\theta_n}\|^2 \le \frac{1}{2}\|\boldsymbol{u}_{n+\theta_n}\|^2. \tag{5.16}$$

In particular,

$$\|\overline{\boldsymbol{u}}_{n+\theta_n}\| \le \|\boldsymbol{u}_{n+\theta_n}\|, \qquad \|\nabla\cdot\overline{\boldsymbol{u}}_{n+\theta_n}\|^2 \le \frac{1}{2\Gamma}\|\boldsymbol{u}_{n+\theta_n}\|^2. \tag{5.17}$$

Step 2: Momentum estimate. Testing the momentum equation in (4.5) with $\tau_n \boldsymbol{u}_{n+\theta_n}$ and applying Lemma 3.1:

$$\begin{aligned} &\frac{1}{2}\big(\|\boldsymbol{u}_{n+1}\|^2 - \|\boldsymbol{u}_n\|^2\big) + \Big(\theta_n - \frac{1}{2}\Big)\|\boldsymbol{u}_{n+1} - \boldsymbol{u}_n\|^2 + \tau_n \int_\Omega \nu(c_{n+\theta_n})\,|D(\boldsymbol{u}_{n+\theta_n})|^2\, d\boldsymbol{x} \\ &\quad + \tau_n\Big[\big((\overline{\boldsymbol{u}}_{n+\theta_n}\cdot\nabla)\boldsymbol{u}_{n+\theta_n}, \boldsymbol{u}_{n+\theta_n}\big)_\Omega + \tfrac{1}{2}\big((\nabla\cdot\overline{\boldsymbol{u}}_{n+\theta_n})\boldsymbol{u}_{n+\theta_n}, \boldsymbol{u}_{n+\theta_n}\big)_\Omega\Big] \\ &= -\tau_n g\big((1+\gamma c_{n+\theta_n})\boldsymbol{i}_2, \boldsymbol{u}_{n+\theta_n}\big)_\Omega + \tau_n(\boldsymbol{f}_{n+\theta_n}, \boldsymbol{u}_{n+\theta_n})_\Omega. \end{aligned}$$

The constant gravity term vanishes: $(\boldsymbol{i}_2, \boldsymbol{u}_{n+\theta_n})_\Omega = (\nabla x_2, \boldsymbol{u}_{n+\theta_n})_\Omega = -(\nabla\cdot\boldsymbol{u}_{n+\theta_n}, x_2)_\Omega + \int_{\partial\Omega}(\boldsymbol{u}_{n+\theta_n}\cdot\boldsymbol{n})\,x_2\,dS = 0$, where we used $\nabla\cdot\boldsymbol{u}_{n+\theta_n} = 0$ and $\boldsymbol{u}_{n+\theta_n} = \boldsymbol{0}$ on $\partial\Omega$. The skew-symmetric convective term vanishes by Lemma 3.3. Therefore:

$$\begin{aligned}\frac{1}{2}\big(\|\boldsymbol{u}_{n+1}\|^2 - \|\boldsymbol{u}_n\|^2\big) + \Big(\theta_n - \frac{1}{2}\Big)\|\boldsymbol{u}_{n+1}-\boldsymbol{u}_n\|^2 + \tau_n\int_\Omega \nu(c_{n+\theta_n})\,|D(\boldsymbol{u}_{n+\theta_n})|^2\,d\boldsymbol{x} \\ = -\tau_n g\gamma(c_{n+\theta_n}, \boldsymbol{u}_{n+\theta_n}\cdot\boldsymbol{i}_2)_\Omega + \tau_n(\boldsymbol{f}_{n+\theta_n}, \boldsymbol{u}_{n+\theta_n})_\Omega.\end{aligned} \tag{5.18}$$

Step 3: Concentration estimate. Testing the concentration equation in (4.5) with $\tau_n c_{n+\theta_n}$ and applying Lemma 3.1:

$$\begin{aligned}&\frac{1}{2}\big(\|c_{n+1}\|^2 - \|c_n\|^2\big) + \Big(\theta_n - \frac{1}{2}\Big)\|c_{n+1}-c_n\|^2 - \tau_n\Theta(\Delta c_{n+\theta_n}, c_{n+\theta_n})_\Omega \\ &\quad + \tau_n(\boldsymbol{u}_{n+\theta_n}\cdot\nabla c_{n+\theta_n}, c_{n+\theta_n})_\Omega + \tau_n U\Big(\frac{\partial c_{n+\theta_n}}{\partial x_2}, c_{n+\theta_n}\Big)_\Omega = 0.\end{aligned}$$

For the diffusion term, integration by parts and the no-flux condition (1.2) give

$$-\Theta(\Delta c_{n+\theta_n}, c_{n+\theta_n})_\Omega = \Theta\|\nabla c_{n+\theta_n}\|^2 - U\int_{\partial\Omega} c_{n+\theta_n}^2\, n_2\,dS.$$

For the swimming term, integration by parts yields

$$U\Big(\frac{\partial c_{n+\theta_n}}{\partial x_2}, c_{n+\theta_n}\Big)_\Omega = \frac{U}{2}\int_{\partial\Omega} c_{n+\theta_n}^2\, n_2\,dS.$$

The boundary contributions combine to $-\frac{U}{2}\int_{\partial\Omega} c_{n+\theta_n}^2\, n_2\,dS$, which equals $U(\nabla c_{n+\theta_n}\cdot\boldsymbol{i}_2, c_{n+\theta_n})_\Omega$ as a volume integral. For the convective term, integration by parts and $\boldsymbol{u}_{n+\theta_n} = \boldsymbol{0}$ on $\partial\Omega$ give

$$(\boldsymbol{u}_{n+\theta_n}\cdot\nabla c_{n+\theta_n}, c_{n+\theta_n})_\Omega = -\frac{1}{2}(\nabla\cdot\boldsymbol{u}_{n+\theta_n}, |c_{n+\theta_n}|^2)_\Omega = 0.$$

The concentration energy balance therefore reads

$$\frac{1}{2}\big(\|c_{n+1}\|^2 - \|c_n\|^2\big) + \Big(\theta_n - \frac{1}{2}\Big)\|c_{n+1}-c_n\|^2 + \tau_n\Theta\|\nabla c_{n+\theta_n}\|^2 = \tau_n U(\nabla c_{n+\theta_n}\cdot\boldsymbol{i}_2, c_{n+\theta_n})_\Omega. \tag{5.19}$$

Step 4: Combining and closing. Adding (5.18) and (5.19):

$$\begin{aligned}&\frac{1}{2}(E_{n+1}-E_n) + \Big(\theta_n - \frac{1}{2}\Big)\big[\|\boldsymbol{u}_{n+1}-\boldsymbol{u}_n\|^2 + \|c_{n+1}-c_n\|^2\big] \\ &\quad + \tau_n\int_\Omega \nu(c_{n+\theta_n})\,|D(\boldsymbol{u}_{n+\theta_n})|^2\,d\boldsymbol{x} + \tau_n\Theta\|\nabla c_{n+\theta_n}\|^2 \\ &= -\tau_n g\gamma(c_{n+\theta_n}, \boldsymbol{u}_{n+\theta_n}\cdot\boldsymbol{i}_2)_\Omega + \tau_n(\boldsymbol{f}_{n+\theta_n}, \boldsymbol{u}_{n+\theta_n})_\Omega + \tau_n U(\nabla c_{n+\theta_n}\cdot\boldsymbol{i}_2, c_{n+\theta_n})_\Omega.\end{aligned}$$

We bound each term on the right-hand side. By Young's inequality and the Korn–Poincaré inequality (Lemma 3.4):

$$\begin{aligned}\tau_n g\gamma\big|(c_{n+\theta_n}, \boldsymbol{u}_{n+\theta_n}\cdot\boldsymbol{i}_2)_\Omega\big| &\le \tau_n g\gamma\Big(\frac{1}{4\varepsilon_1}\|c_{n+\theta_n}\|^2 + \varepsilon_1 C_K^2\|D(\boldsymbol{u}_{n+\theta_n})\|^2\Big), \\ \tau_n\big|(\boldsymbol{f}_{n+\theta_n}, \boldsymbol{u}_{n+\theta_n})_\Omega\big| &\le \tau_n\Big(\frac{1}{4\varepsilon_2}\|\boldsymbol{f}_{n+\theta_n}\|^2 + \varepsilon_2 C_K^2\|D(\boldsymbol{u}_{n+\theta_n})\|^2\Big), \\ \tau_n U\big|(\nabla c_{n+\theta_n}\cdot\boldsymbol{i}_2, c_{n+\theta_n})_\Omega\big| &\le \tau_n U\Big(\frac{1}{4\varepsilon_3}\|c_{n+\theta_n}\|^2 + \varepsilon_3\|\nabla c_{n+\theta_n}\|^2\Big).\end{aligned}$$

Choosing

$$\varepsilon_1 = \frac{\nu_*}{2g\gamma C_K^2}, \qquad \varepsilon_2 = \frac{\nu_*}{2C_K^2}, \qquad \varepsilon_3 = \frac{\Theta}{2U},$$

and absorbing the dissipation and diffusion terms into the left-hand side, we derive

$$\begin{aligned}&\frac{1}{2}(E_{n+1}-E_n)+\frac{2\theta_n-1}{2}\left[\|\boldsymbol{u}_{n+1}-\boldsymbol{u}_n\|^2+\|c_{n+1}-c_n\|^2\right]\\&\quad+\tau_n\int_\Omega(\nu(c_{n+\theta_n})-\nu_*)\,|D(\boldsymbol{u}_{n+\theta_n})|^2\,d\boldsymbol{x}+\tau_n\frac{\Theta}{2}\|\nabla c_{n+\theta_n}\|^2\\&\le\tau_n\left(g^2\gamma^2\frac{C_K^2}{2\nu_*}+\frac{U^2}{2\Theta}\right)\|c_{n+\theta_n}\|^2+\tau_n\frac{C_K^2}{2\nu_*}\|\boldsymbol{f}_{n+\theta_n}\|^2.\end{aligned}\tag{5.20}$$

By Lemma 3.2, $\|c_{n+\theta_n}\|^2\le E_{n+1}+E_n$. With M defined by (5.14), the right-hand side of (5.20) is bounded by

$$\tau_n\frac{M}{2}(E_{n+1}+E_n)+\tau_n\frac{C_K^2}{2\nu_*}\|\boldsymbol{f}_{n+\theta_n}\|^2.$$

Dropping the non-negative dissipation and diffusion terms from the left-hand side:

$$E_{n+1}-E_n\le\tau_nM(E_{n+1}+E_n)+\tau_n\frac{C_K^2}{\nu_*}\|\boldsymbol{f}_{n+\theta_n}\|^2.\tag{5.21}$$

Rearranging:

$$(1-\tau_nM)\,E_{n+1}\le(1+\tau_nM)\,E_n+\tau_n\frac{C_K^2}{\nu_*}\|\boldsymbol{f}_{n+\theta_n}\|^2.$$

Under (5.14), $1-\tau_nM\ge\frac{1}{2}>0$. Using $\frac{1+x}{1-x}\le1+4x$ and $\frac{1}{1-x}\le2$ for $0\le x\le\frac{1}{2}$:

$$E_{n+1}\le(1+4\tau_nM)\,E_n+\frac{2C_K^2}{\nu_*}\,\tau_n\|\boldsymbol{f}_{n+\theta_n}\|^2.$$

Applying Lemma 3.6:

$$E_N\le e^{4MT}\left(E_0+\frac{2C_K^2}{\nu_*}\sum_{n=0}^{N-1}\tau_n\|\boldsymbol{f}_{n+\theta_n}\|^2\right).\tag{5.22}$$

Returning to (5.20) and summing from $n=0$ to $N-1$ yields (5.15). □

REMARK 6. *we note that the method has nonzero numerical dissipation unless $\theta_n=1/2$, which corresponds to the midpoint rule.*

6. Spatial discretization and filter parameters. In this section, we describe the spatial discretization of the semi-discrete system (4.4) and analyze the effect of the grad-div filter parameters Γ and χ. As shown in [30, 40], the condition number of the grad-div filter (1.7) scales as $\mathscr{O}(\Gamma/\chi)$. The authors also report that the accuracy of the filtered velocity improves as Γ increases, and they use large values of Γ in their numerical experiments. We provide a theoretical explanation for this observation at the continuous level by showing that the discrepancy between the grad-div filter (1.7) and the Stokes-type filter (1.6) is bounded by $\mathscr{O}(\Gamma^{-1/2})$.

At the discrete level, however, the situation is more subtle. The discrete Stokes-type filter enforces incompressibility only in the pressure space, so the filtered velocity is generally not pointwise divergence-free. We show that the corresponding error estimate contains competing terms that increase with Γ. As a result, choosing Γ too large may degrade the overall accuracy of the discrete filter. This analysis provides a theoretical basis for selecting a suitable range of values for Γ and χ, rather than taking Γ arbitrarily large. Numerical experiments supporting these conclusions are presented in Section 7.

6.1. The fully discrete numerical method. Let $\mathscr{T}_h$ be a shape-regular triangulation of Ω with mesh size h. We choose conforming finite element spaces

$$\boldsymbol{V}_h\subset\boldsymbol{V},\qquad Q_h\subset Q,\qquad S_h\subset S.$$

We employ Taylor–Hood elements for the velocity–pressure pair and continuous piecewise polynomials for the concentration:

$$\begin{aligned}\boldsymbol{V}_h &= \{\boldsymbol{v}_h \in \boldsymbol{V} : \boldsymbol{v}_h|_K \in [\mathbb{P}_k(K)]^d,\ \forall K \in \mathscr{T}_h\},\\ Q_h &= \{q_h \in Q : q_h|_K \in \mathbb{P}_{k-1}(K),\ \forall K \in \mathscr{T}_h\},\\ S_h &= \{s_h \in S : s_h|_K \in \mathbb{P}_k(K),\ \forall K \in \mathscr{T}_h\}.\end{aligned}$$

The fully discrete method is obtained by replacing $\boldsymbol{V}$, Q, and S in the decoupled subiteration (4.1)–(4.3) with $\boldsymbol{V}_h$, Q_h, and S_h, respectively.

6.2. Choice of the filter parameters. The grad-div filter (2.2) avoids the solution of a mixed saddle-point problem by relaxing the incompressibility constraint through grad-div penalization. We now quantify the error introduced by this approximation relative to the Stokes-type filter (1.6), at both the continuous and discrete levels.

Continuous-level estimate.. At the continuous level, let $(\overline{\boldsymbol{u}}_S, \lambda) \in \boldsymbol{V} \times Q$ solve the Stokes-type filter:

$$-\alpha^2 \nabla \cdot (a \nabla \overline{\boldsymbol{u}}_S) + \overline{\boldsymbol{u}}_S + \nabla \lambda = \boldsymbol{u}, \qquad \nabla \cdot \overline{\boldsymbol{u}}_S = 0 \quad \text{in } \Omega, \qquad \overline{\boldsymbol{u}}_S = \boldsymbol{u} \quad \text{on } \partial\Omega, \tag{6.1}$$

and let $\overline{\boldsymbol{u}}_G \in \boldsymbol{V}$ solve the grad-div filter:

$$-\alpha^2 \nabla \cdot (a \nabla \overline{\boldsymbol{u}}_G) + \overline{\boldsymbol{u}}_G - \Gamma \nabla \nabla \cdot \overline{\boldsymbol{u}}_G = \boldsymbol{u} \quad \text{in } \Omega, \qquad \overline{\boldsymbol{u}}_G = \boldsymbol{u} \quad \text{on } \partial\Omega. \tag{6.2}$$

Since the continuous velocity satisfies $\nabla \cdot \boldsymbol{u} = 0$, the term $\chi \nabla \nabla \cdot \boldsymbol{u}$ vanishes at the continuous level.

PROPOSITION 6.1. *Under Assumption 2, let $\boldsymbol{e} = \overline{\boldsymbol{u}}_S - \overline{\boldsymbol{u}}_G$. Then*

$$\alpha^2 a_{\min} \|\nabla \boldsymbol{e}\|^2 + \|\boldsymbol{e}\|^2 + \frac{\Gamma}{2} \|\nabla \cdot \overline{\boldsymbol{u}}_G\|^2 \le \frac{1}{2\Gamma} \|\lambda\|^2. \tag{6.3}$$

Proof. Subtracting (6.2) from (6.1), we obtain

$$-\alpha^2 \nabla \cdot (a \nabla \boldsymbol{e}) + \boldsymbol{e} + \nabla \lambda + \Gamma \nabla \nabla \cdot \overline{\boldsymbol{u}}_G = \boldsymbol{0}.$$

Testing with $\boldsymbol{e}$ gives

$$\alpha^2 (a \nabla \boldsymbol{e}, \nabla \boldsymbol{e}) + \|\boldsymbol{e}\|^2 + (\nabla \lambda, \boldsymbol{e}) + \Gamma (\nabla \nabla \cdot \overline{\boldsymbol{u}}_G, \boldsymbol{e}) = 0.$$

Since $\boldsymbol{e} = 0$ on $\partial\Omega$, integration by parts yields

$$\alpha^2 (a \nabla \boldsymbol{e}, \nabla \boldsymbol{e}) + \|\boldsymbol{e}\|^2 - (\lambda, \nabla \cdot \boldsymbol{e}) - \Gamma (\nabla \cdot \overline{\boldsymbol{u}}_G, \nabla \cdot \boldsymbol{e}) = 0.$$

Because $\nabla \cdot \overline{\boldsymbol{u}}_S = 0$, we have

$$\nabla \cdot \boldsymbol{e} = \nabla \cdot (\overline{\boldsymbol{u}}_S - \overline{\boldsymbol{u}}_G) = -\nabla \cdot \overline{\boldsymbol{u}}_G.$$

Therefore,

$$\alpha^2 (a \nabla \boldsymbol{e}, \nabla \boldsymbol{e}) + \|\boldsymbol{e}\|^2 + (\lambda, \nabla \cdot \overline{\boldsymbol{u}}_G) + \Gamma \|\nabla \cdot \overline{\boldsymbol{u}}_G\|^2 = 0.$$

Using Assumption 2, we obtain

$$\alpha^2 a_{\min} \|\nabla \boldsymbol{e}\|^2 + \|\boldsymbol{e}\|^2 + \Gamma \|\nabla \cdot \overline{\boldsymbol{u}}_G\|^2 \le \|\lambda\| \, \|\nabla \cdot \overline{\boldsymbol{u}}_G\|.$$

Applying Young's inequality,

$$\|\lambda\| \, \|\nabla \cdot \overline{\boldsymbol{u}}_G\| \le \frac{1}{2\Gamma} \|\lambda\|^2 + \frac{\Gamma}{2} \|\nabla \cdot \overline{\boldsymbol{u}}_G\|^2,$$

and absorbing the last term into the left-hand side completes the proof. ∎

REMARK 7. *Estimate (6.3) shows that the grad-div filter provides a close approximation to the Stokes-type filter for sufficiently large Γ. This gives a theoretical explanation for the numerical observation in [40] that increasing Γ leads to a more accurate filtered velocity.*

Discrete-level estimate.. At the discrete level, the situation is more subtle. Let $(\overline{\boldsymbol{u}}_S^h, \lambda_h) \in \boldsymbol{V}_h \times Q_h$ solve the discrete Stokes-type filter: for all $(\boldsymbol{v}_h, q_h) \in \boldsymbol{V}_h \times Q_h$,

$$\begin{aligned} \alpha^2(a\nabla\overline{\boldsymbol{u}}_S^h, \nabla\boldsymbol{v}_h) + (\overline{\boldsymbol{u}}_S^h, \boldsymbol{v}_h) - (\lambda_h, \nabla\cdot\boldsymbol{v}_h) &= (\boldsymbol{u}_h, \boldsymbol{v}_h), \\ (\nabla\cdot\overline{\boldsymbol{u}}_S^h, q_h) &= 0, \end{aligned} \tag{6.4}$$

and let $\overline{\boldsymbol{u}}_G^h \in \boldsymbol{V}_h$ solve the discrete grad-div filter: for all $\boldsymbol{v}_h \in \boldsymbol{V}_h$,

$$\alpha^2(a\nabla\overline{\boldsymbol{u}}_G^h, \nabla\boldsymbol{v}_h) + (\overline{\boldsymbol{u}}_G^h, \boldsymbol{v}_h) + \Gamma(\nabla\cdot\overline{\boldsymbol{u}}_G^h, \nabla\cdot\boldsymbol{v}_h) = (\boldsymbol{u}_h, \boldsymbol{v}_h) + \chi(\nabla\cdot\boldsymbol{u}_h, \nabla\cdot\boldsymbol{v}_h). \tag{6.5}$$

Although $\overline{\boldsymbol{u}}_S^h$ is weakly divergence-free, its pointwise divergence generally does not vanish. Similarly, the discrete velocity $\boldsymbol{u}_h$ may have a nonzero divergence residual. These residuals are responsible for the additional terms in the following estimate.

LEMMA 6.2. *Under Assumption 2, let* $\boldsymbol{e}_h := \overline{\boldsymbol{u}}_S^h - \overline{\boldsymbol{u}}_G^h$. *Then*

$$\alpha^2 a_{\min}\|\nabla\boldsymbol{e}_h\|^2 + \|\boldsymbol{e}_h\|^2 + \frac{\Gamma}{4}\|\nabla\cdot\overline{\boldsymbol{u}}_G^h\|^2 \le \frac{1}{\Gamma}\|\lambda_h\|^2 + \left(\Gamma + \frac{\chi}{2}\right)\|\nabla\cdot\overline{\boldsymbol{u}}_S^h\|^2 + \left(\frac{\chi^2}{\Gamma} + \frac{\chi}{2}\right)\|\nabla\cdot\boldsymbol{u}_h\|^2. \tag{6.6}$$

Proof. Subtracting (6.5) from (6.4) and taking $\boldsymbol{v}_h = \boldsymbol{e}_h$ gives

$$\alpha^2(a\nabla\boldsymbol{e}_h, \nabla\boldsymbol{e}_h) + \|\boldsymbol{e}_h\|^2 - (\lambda_h, \nabla\cdot\boldsymbol{e}_h) - \Gamma(\nabla\cdot\overline{\boldsymbol{u}}_G^h, \nabla\cdot\boldsymbol{e}_h) = -\chi(\nabla\cdot\boldsymbol{u}_h, \nabla\cdot\boldsymbol{e}_h).$$

Since $\nabla\cdot\boldsymbol{e}_h = \nabla\cdot\overline{\boldsymbol{u}}_S^h - \nabla\cdot\overline{\boldsymbol{u}}_G^h$, and since $\lambda_h \in Q_h$, the discrete divergence constraint gives $(\lambda_h, \nabla\cdot\overline{\boldsymbol{u}}_S^h) = 0$. Therefore,

$$(\lambda_h, \nabla\cdot\boldsymbol{e}_h) = -(\lambda_h, \nabla\cdot\overline{\boldsymbol{u}}_G^h).$$

Expanding the remaining divergence terms yields

$$\begin{aligned} &\alpha^2(a\nabla\boldsymbol{e}_h, \nabla\boldsymbol{e}_h) + \|\boldsymbol{e}_h\|^2 + \Gamma\|\nabla\cdot\overline{\boldsymbol{u}}_G^h\|^2 \\ &\quad = -(\lambda_h, \nabla\cdot\overline{\boldsymbol{u}}_G^h) + \Gamma(\nabla\cdot\overline{\boldsymbol{u}}_G^h, \nabla\cdot\overline{\boldsymbol{u}}_S^h) + \chi(\nabla\cdot\boldsymbol{u}_h, \nabla\cdot\overline{\boldsymbol{u}}_G^h) - \chi(\nabla\cdot\boldsymbol{u}_h, \nabla\cdot\overline{\boldsymbol{u}}_S^h). \end{aligned}$$

Using Assumption 2, we infer that

$$\begin{aligned} &\alpha^2 a_{\min}\|\nabla\boldsymbol{e}_h\|^2 + \|\boldsymbol{e}_h\|^2 + \Gamma\|\nabla\cdot\overline{\boldsymbol{u}}_G^h\|^2 \\ &\quad \le \|\lambda_h\|\,\|\nabla\cdot\overline{\boldsymbol{u}}_G^h\| + \Gamma\|\nabla\cdot\overline{\boldsymbol{u}}_G^h\|\,\|\nabla\cdot\overline{\boldsymbol{u}}_S^h\| + \chi\|\nabla\cdot\boldsymbol{u}_h\|\,\|\nabla\cdot\overline{\boldsymbol{u}}_G^h\| + \chi\|\nabla\cdot\boldsymbol{u}_h\|\,\|\nabla\cdot\overline{\boldsymbol{u}}_S^h\|. \end{aligned}$$

Applying Young's inequality to the four terms on the right-hand side, we obtain

$$\begin{aligned} \|\lambda_h\|\,\|\nabla\cdot\overline{\boldsymbol{u}}_G^h\| &\le \frac{1}{\Gamma}\|\lambda_h\|^2 + \frac{\Gamma}{4}\|\nabla\cdot\overline{\boldsymbol{u}}_G^h\|^2, \\ \Gamma\|\nabla\cdot\overline{\boldsymbol{u}}_G^h\|\,\|\nabla\cdot\overline{\boldsymbol{u}}_S^h\| &\le \Gamma\|\nabla\cdot\overline{\boldsymbol{u}}_S^h\|^2 + \frac{\Gamma}{4}\|\nabla\cdot\overline{\boldsymbol{u}}_G^h\|^2, \\ \chi\|\nabla\cdot\boldsymbol{u}_h\|\,\|\nabla\cdot\overline{\boldsymbol{u}}_G^h\| &\le \frac{\chi^2}{\Gamma}\|\nabla\cdot\boldsymbol{u}_h\|^2 + \frac{\Gamma}{4}\|\nabla\cdot\overline{\boldsymbol{u}}_G^h\|^2, \\ \chi\|\nabla\cdot\boldsymbol{u}_h\|\,\|\nabla\cdot\overline{\boldsymbol{u}}_S^h\| &\le \frac{\chi}{2}\|\nabla\cdot\boldsymbol{u}_h\|^2 + \frac{\chi}{2}\|\nabla\cdot\overline{\boldsymbol{u}}_S^h\|^2. \end{aligned}$$

Substituting these bounds into the previous inequality and absorbing the three $\frac{\Gamma}{4}\|\nabla\cdot\overline{\boldsymbol{u}}_G^h\|^2$ terms into the left-hand side gives (6.6). ∎

REMARK 8. *The continuous estimate (6.3) suggests that increasing* Γ *improves the approximation of the Stokes-type filter. The discrete estimate (6.6), however, reveals a competing effect: terms involving the discrete divergence residuals are amplified by* Γ *and* χ. *Therefore, in computations,* Γ *should be chosen large enough to improve the incompressibility of the filtered velocity, but not so large that it magnifies the divergence error of the discrete approximation.*

7. Numerical simulations. In this section, we present computational results that demonstrate the effectiveness of the proposed adaptive filtered method. We first verify the spatial and temporal convergence rates in both two and three dimensions using a manufactured solution. We then examine the effect of the grad-div filter parameters Γ and χ, as predicted by the analysis in Section 6. Next, we present bioconvection simulations at moderate and high Rayleigh numbers, comparing the filtered method on coarse meshes with the standard unfiltered method on both coarse and fine meshes. Finally, we consider a concentration-dependent viscosity case to test the method in a nonlinear viscosity regime. Although the time-discretization framework allows variable time steps, all numerical experiments reported below use a uniform time step $\tau_n = \Delta t$. The convergence tests for the manufactured solution use Dirichlet boundary data prescribed from the exact solution. In all remaining bioconvection simulations, periodic boundary conditions are imposed in the horizontal direction, with no-slip velocity boundary conditions and no-flux concentration boundary conditions on the top and bottom boundaries.

In all of our simulations, we adopt an indicator function based on approximate deconvolution [7]:

$$a(\boldsymbol{u}) = \frac{|\boldsymbol{u} - \overline{\boldsymbol{u}}_H|}{\max\left(||\boldsymbol{u} - \overline{\boldsymbol{u}}_H||_{L^\infty(\Omega)}, 1\right)}, \tag{7.1}$$

where $\overline{\boldsymbol{u}}_H$ is the Helmholtz filter of $\boldsymbol{u}$ without the enforcement of the incompressibility constraint:

$$-\alpha^2 \Delta \overline{\boldsymbol{u}}_H + \overline{\boldsymbol{u}}_H = \boldsymbol{u} \quad \text{in} \quad \Omega, \qquad \overline{\boldsymbol{u}}_H = \boldsymbol{u} \quad \text{on} \quad \partial\Omega. \tag{7.2}$$

All numerical experiments use Taylor–Hood (P_2, P_1) finite elements for the velocity–pressure pair and continuous P_2 finite elements for the concentration.

All computations are carried out in the Julia programming language [6] using the Gridap finite element library [2, 43], together with GridapSolvers [32] and the `DataStructures.jl` package [24]. All computations are performed on the Center for Research Computing (CRC) cluster at the University of Notre Dame. Reported computational times are measured on the same hardware configuration to ensure a fair comparison between methods.

7.1. Convergence study in 2D and 3D. We first verify the spatial and temporal convergence rates on the square domain $\Omega = [-1,1]^2$ for the filtered bioconvection system (2.1) with $T = 1$. The parameters are fixed as

$$g = 10, \quad \gamma = 0.1, \quad \nu = 0.1, \quad \Theta = 0.1, \quad U = 0.1.$$

For the filtered solver, we set $\alpha = 0.1\,h, \Gamma = 2$ and $\chi = 1$. The non-filtered solver is recovered by setting $\alpha = \Gamma = \chi = 0$. The exact solution is given by

$$\boldsymbol{u} = \left(t^2 \sin(\pi x)\cos(\pi y), -t^2 \cos(\pi x)\sin(\pi y)\right), \qquad p = t^2 x^2 y^2, \qquad c = t^2 x^2 y^2.$$

At each time step, the Dirichlet boundary conditions for the velocity and concentration are prescribed using the traces of the exact solution. We choose $\theta = 1/2$, and take the initial data to be the L^2 projection of continuous solutions into the finite element space. We calculate the forcing term $\boldsymbol{f}$ using the exact solution, and in the same way we add and calculate the forcing term in the concentration equation.

Using Algorithm 1, we compute solutions on five successive mesh and time step refinements with $\Delta t = O(h)$. Figure 7.1(a) shows the L^2 errors for the velocity and concentration as functions of the mesh size, for both the filtered and non-filtered solvers. Both methods achieve second-order convergence. The filtered solver produces errors of comparable magnitude to the non-filtered solver, confirming that the adaptive filtering does not degrade the accuracy of the spatial discretization.

We repeat the experiment in three dimensions on the domain $\Omega = [-1,1]^3$ with the manufactured solution

$$\boldsymbol{u} = \left(t^2 \sin(\pi x)\cos(\pi y)\cos(\pi z), -2t^2 \cos(\pi x)\sin(\pi y)\cos(\pi z), t^2 \cos(\pi x)\cos(\pi y)\sin(\pi z)\right),$$
$$p = t^2 \sin(\pi x)\cos(\pi y)\sin(\pi z), \qquad c = t^2 x^2 y^2 z^2.$$

with the same physical and filter parameters. Four successive refinement levels are used. As shown in Figure 7.1(b), second-order convergence is again observed for both solvers, confirming that the method and its convergence properties extend to three dimensions.

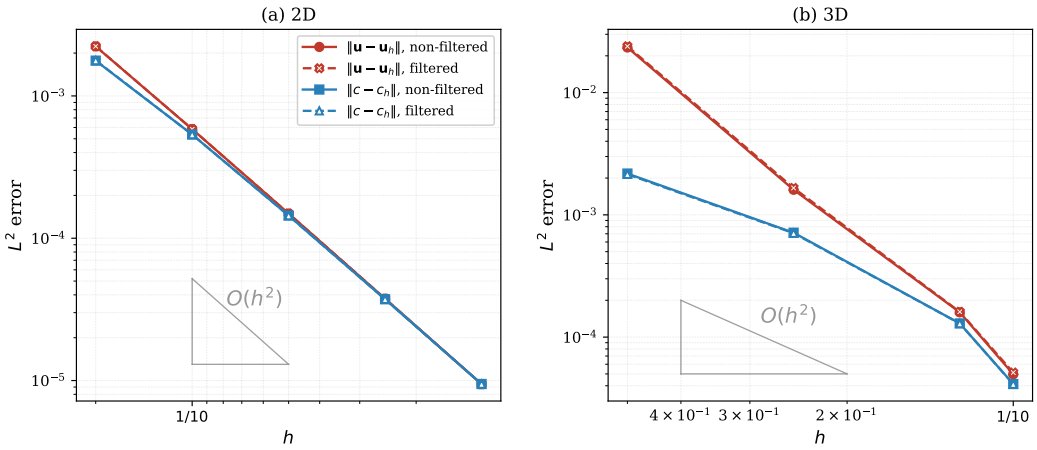

Fig. 7.1: L^2 convergence rates for velocity and concentration in (a) 2D, and (b) 3D. Solid lines: non-filtered solver ($\alpha=\Gamma=\chi=0$); dashed lines: filtered solver ($\alpha=0.1\,h$, $\Gamma=2$, $\chi=1$). Both solvers achieve second-order convergence.

7.2. The effect of the grad-div filter parameters. The grad-div filter (1.7) approximates the Stokes-type filter (1.6) by relaxing the divergence-free constraint and enforcing it through a penalty term. This avoids solving a mixed saddle-point problem and reduces the computational cost. We assess the quality of this approximation using two criteria: the discrepancy from the Stokes-type filtered velocity and the divergence residual of the grad-div filtered velocity. These quantities were analyzed in Section 6. Here, we examine their behavior numerically.

The discrete estimate (6.6) reveals competing effects in the choice of the grad-div parameters Γ and χ. Since the condition number of the filter system scales with the ratio $r=\Gamma/\chi$, we vary χ while keeping r fixed and setting $\Gamma=r\chi$. Under this choice, the upper bound contains terms that decrease with χ and terms that increase with χ, suggesting that an intermediate range may provide a favorable filter-level balance.

The simulations are conducted on the domain $\Omega=[0,L]\times[0,H]$, with $L=16$ and $H=2$. The physical parameters are fixed as

$$g=980.665,\qquad \gamma=0.1,\qquad \nu=0.1,\qquad \Theta=0.1,\qquad U=0.1.$$

We first solve the unfiltered bioconvection system (1.1), corresponding to $\alpha=\Gamma=\chi=0$, with final time $T=35$, time step $\Delta t=0.01$, and mesh size $h=0.1$. The initial data are

$$\boldsymbol{u}_0=\mathbf{0},\qquad c_0=10^6.$$

We then use the computed velocity field at the final time $T=35$ as the input to both the discrete Stokes-type filter (1.6) and the discrete grad-div filter (1.7). Thus, the filtered velocities $\overline{\boldsymbol{u}}_S^h$ and $\overline{\boldsymbol{u}}_G^h$ are computed in post-processing from the same discrete velocity field. The filter radius is fixed at $\alpha=0.05$. For each fixed ratio $r=\Gamma/\chi$, we vary χ and set $\Gamma=r\chi$. We monitor the filter discrepancy and the divergence residual:

$$E_{\text{filter}}=\|\overline{\boldsymbol{u}}_S^h-\overline{\boldsymbol{u}}_G^h\|_{L^2},\qquad E_{\text{div}}=\|\nabla\cdot\overline{\boldsymbol{u}}_G^h\|_{L^2}.$$

Figure 7.2 displays the results. For each fixed r, increasing χ (and hence Γ) slightly reduces the divergence residual E_{div} (right panel) but increases the discrepancy E_{filter} (left panel). The dependence on the ratio r is more pronounced. Larger values of r substantially improve divergence control but also increase the distance from the Stokes-type filtered velocity. These results are consistent with the competing effects predicted by the discrete estimate (6.6) and suggest that the filter parameters should be selected by balancing divergence control against agreement with the Stokes-type filter, rather than by minimizing either quantity alone.

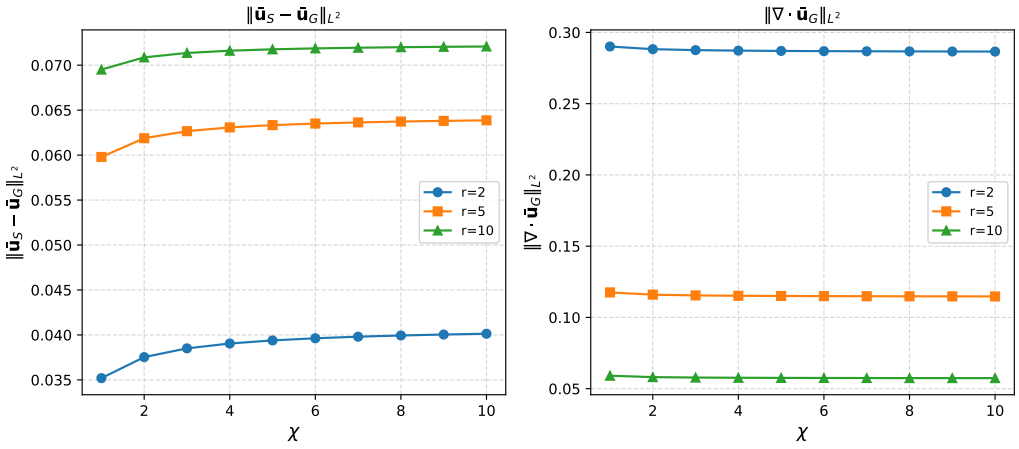

Fig. 7.2: Effects of the grad-div parameters on the discrete filter approximation. For each fixed ratio $r = \Gamma/\chi$, we vary χ and set $\Gamma = r\chi$. The discrepancy between the discrete Stokes-type and grad-div filtered velocities (left panel) increases with both χ and r, while the divergence residual of the grad-div filtered velocity (right panel) decreases.

7.3. Constant-viscosity bioconvection simulations. In this subsection, we investigate the performance of the adaptive filtered method in two-dimensional bioconvection simulations. We compare the filtered method on a coarse mesh with the standard unfiltered method on both coarse and fine meshes. The fine-mesh unfiltered computation is used as a reference. We examine the resulting plume structures, the evolution of the kinetic and potential energies, mass conservation, and the computational cost. Two regimes are considered, a moderate-Rayleigh case and a high-Rayleigh case.

The simulations are conducted on the domain $\Omega = [0,16] \times [0,2]$. The physical parameters are fixed as

$$g = 980.665, \qquad \gamma = 0.1, \qquad \nu = 0.1, \qquad \Theta = 0.1, \qquad U = 0.1.$$

We vary the Rayleigh number by changing the total initial microorganism mass M_0. The moderate-Rayleigh case corresponds to $M_0 = |\Omega| \times 10^6$, while the high-Rayleigh case corresponds to $M_0 = |\Omega| \times 10^7$. For both cases, we take $T = 200, \Delta t = 0.01$, with initial data

$$\boldsymbol{u}_0 = \mathbf{0}, \qquad c_0 = \frac{M_0}{|\Omega|}.$$

The standard method is recovered by setting $\alpha = \Gamma = \chi = 0$, whereas the filtered method solves (2.1) with the parameters specified below.

Moderate Rayleigh number.. We first consider $M_0 = |\Omega| \times 10^6$. Three computations are compared:

1. the unfiltered method on a coarse mesh with $h = 0.1$;
2. the unfiltered method on a fine mesh with $h = 0.025$;
3. the adaptive filtered method on the coarse mesh with $h = 0.1$, $\alpha = 0.05$, $\Gamma = 10$, $\chi = 0$.

Figure 7.3 compares the microorganism concentration fields at selected times. The coarse-mesh unfiltered computation captures the general plume formation mechanism but differs noticeably from the fine-mesh reference. In contrast, the coarse-mesh filtered computation reproduces the dominant plume structures of the fine-mesh solution more accurately.

Figure 7.4 shows the evolution of the kinetic and potential energies. After an initial transient, the filtered coarse-mesh computation closely follows the fine-mesh reference, while the unfiltered coarse-mesh solution exhibits a more visible discrepancy. The energy traces display persistent long-time fluctuations associated with the evolving plume dynamics. The total microorganism mass is conserved to machine precision at every time step, consistent with Proposition 5.1.

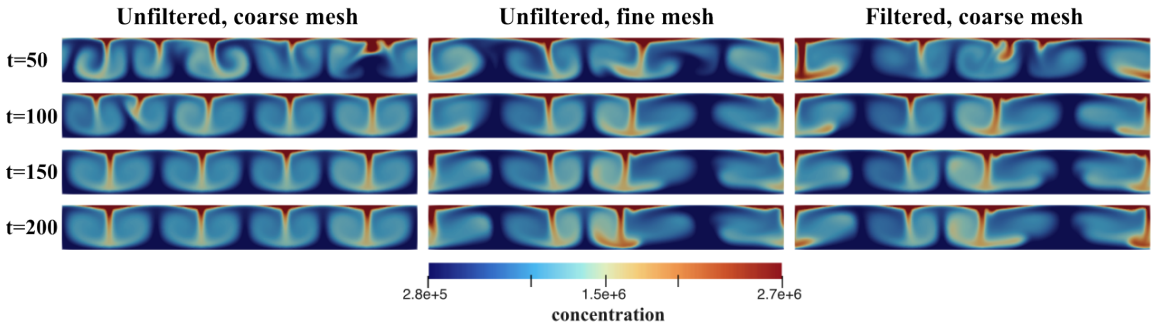

Fig. 7.3: Microorganism concentration fields in the moderate-Rayleigh regime at $t = 50, 100, 150, 200$. Columns from left to right: unfiltered method on the coarse mesh, unfiltered method on the fine mesh, adaptive filtered method on the coarse mesh. The filtered coarse-mesh solution captures the dominant plume structures of the fine-mesh reference more accurately than the unfiltered coarse-mesh solution.

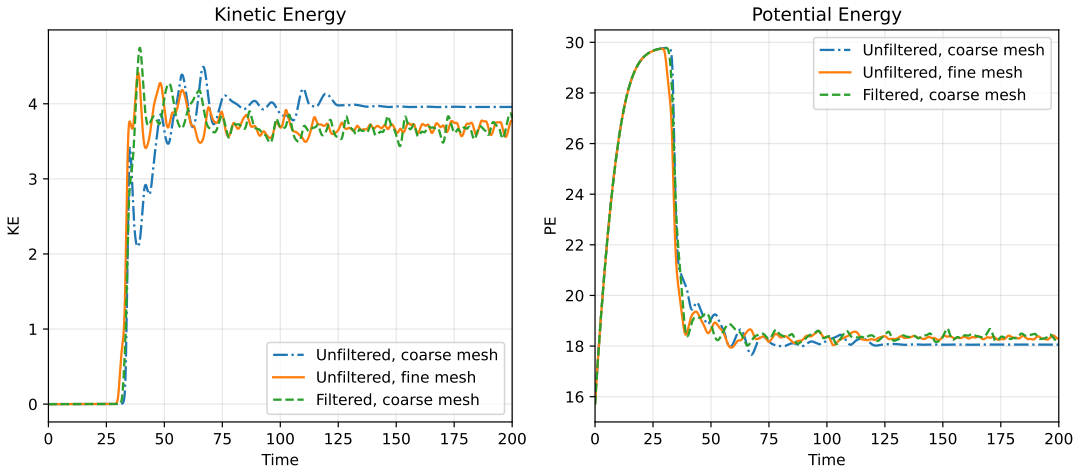

Fig. 7.4: Evolution of the kinetic energy $\mathrm{KE}(t)$ and potential energy $\mathrm{PE}(t)$ in the moderate-Rayleigh regime. The adaptive filtered method on the coarse mesh closely reproduces the energy behavior of the fine-mesh unfiltered reference computation.

Table 7.1 reports the computational cost of the three simulations. Since the unfiltered and filtered methods use different numbers of MPI ranks, we report both wall-clock time and core-hours. The filtered coarse-mesh computation delivers a substantially more accurate approximation of the fine-mesh reference in roughly one-third the wall-clock time (6.5 vs. 17.5 hours).

High Rayleigh number.. We next increase the initial concentration to $M_0 = |\Omega| \times 10^7$. Three computations are compared:

1. the unfiltered method on a coarse mesh with $h = 0.1$;
2. the unfiltered method on a fine mesh with $h = 0.025$;
3. the adaptive filtered method on the coarse mesh with $h = 0.1$, $\alpha = 0.1$, $\Gamma = 100$, $\chi = 10$.

Figure 7.5 compares the concentration fields obtained by the three methods. As the Rayleigh number increases, the plume dynamics become more complex and the discrepancy between the two unfiltered computations becomes more pronounced. The filtered coarse-mesh solution captures the dominant structures of the fine-mesh reference more accurately than the unfiltered solution on the same coarse mesh. Mass conservation is again verified to machine precision.

Table 7.1: Computational cost for the moderate-Rayleigh simulations.

Method	Mesh size h	MPI ranks	Wall-clock time	Core-hours
Unfiltered, coarse mesh	0.1	2	2 hours	4 hours
Unfiltered, fine mesh	0.025	2	17.5 hours	35 hours
Filtered, coarse mesh	0.1	4	6.5 hours	26 hours

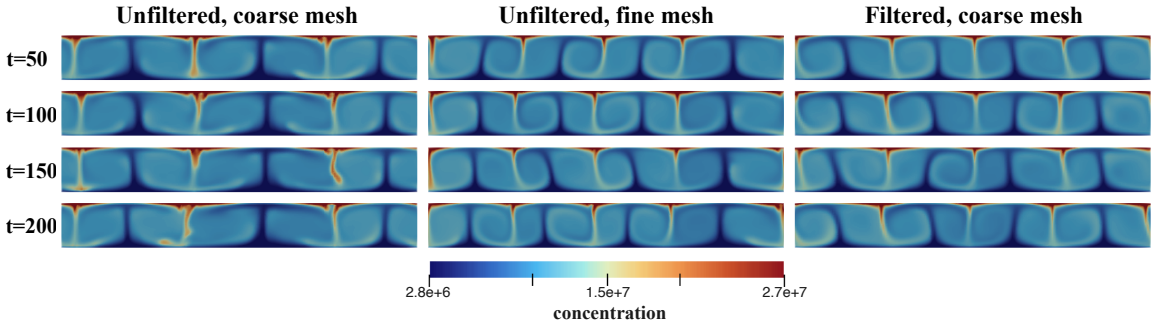

Fig. 7.5: Microorganism concentration fields in the high-Rayleigh regime at $t = 50, 100, 150, 200$. Columns from left to right: unfiltered method on the coarse mesh, unfiltered method on the fine mesh, adaptive filtered method on the coarse mesh. The filtered coarse-mesh solution captures the dominant plume structures of the fine-mesh reference more accurately than the unfiltered coarse-mesh solution.

Figure 7.6 shows the corresponding kinetic- and potential-energy histories. In this regime, the energy traces exhibit stronger and more irregular fluctuations. The adaptive filtered method still provides an improved coarse-mesh approximation of the long-time energy behavior compared with the unfiltered method.

Table 7.2 reports the computational cost of the three simulations. As in the moderate-Rayleigh case, the filtered coarse-mesh computation achieves a more accurate approximation of the fine-mesh reference at a lower cost.

7.4. Concentration-dependent viscosity bioconvection simulations. We next consider a case in which the viscosity depends on the microorganism concentration. This experiment tests the proposed method in a nonlinear viscosity regime and examines whether the adaptive filtered method on a coarse mesh can still reproduce the dominant dynamics of the standard unfiltered method on a fine mesh. We use the following concentration-dependent viscosity law:

$$\nu(c) = \begin{cases} \nu_0, & c_r \le 0, \\ \nu_0 \left(1 + 2.5\, c_r + 5.3\, c_r^2\right), & c_r > 0, \end{cases} \tag{7.3}$$

where $c_r = c/c_{\max}$ is the relative concentration and $c_{\max} = 3 \cdot 10^8$. This constitutive relation is based on the low-concentration expansion for suspensions given in [3]. The remaining physical and numerical parameters are the same as in the moderate-Rayleigh constant-viscosity case. Three computations are compared:

1. the unfiltered method on a coarse mesh with $h = 0.1$;
2. the unfiltered method on a fine mesh with $h = 0.025$;
3. the adaptive filtered method on the coarse mesh with $h = 0.1$, $\alpha = 0.1$, $\Gamma = 16$, $\chi = 0$.

Figure 7.7 compares the microorganism concentration fields at selected times. The concentration-dependent viscosity modifies the plume evolution, but the filtered coarse-mesh computation still captures the dominant plume structures observed in the fine-mesh unfiltered reference. Because periodic boundary conditions are imposed in the horizontal direction, the plume locations may differ by a small horizontal phase shift. Up to this periodic translation, the filtered solution reproduces the main large-scale structures more accurately than the unfiltered solution on the same coarse mesh.

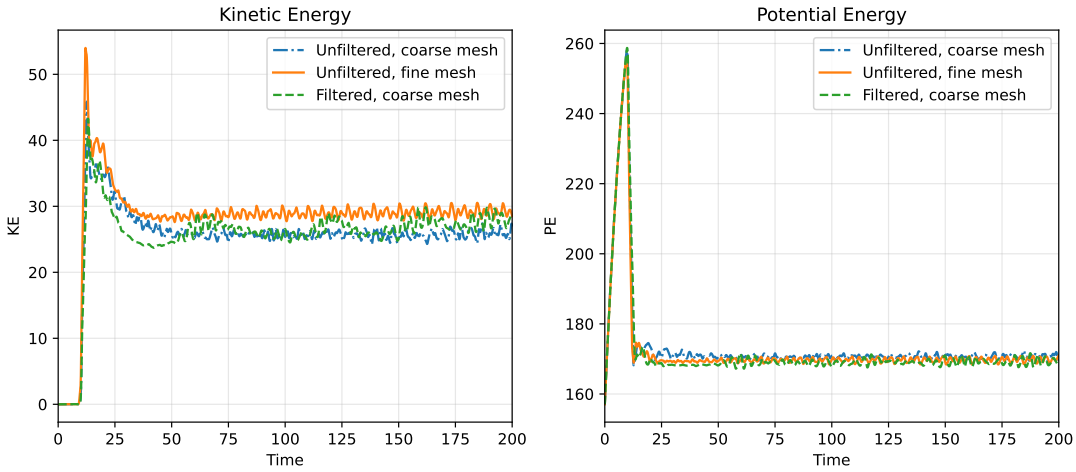

Fig. 7.6: Evolution of the kinetic energy KE(t) and potential energy PE(t) in the high-Rayleigh regime. The adaptive filtered method improves the coarse-mesh approximation of the long-time energy behavior.

Table 7.2: Computational cost for the high-Rayleigh simulations.

Method	Mesh size h	MPI ranks	Wall-clock time	Core-hours
Unfiltered, coarse mesh	0.1	2	3.5 hours	7 hours
Unfiltered, fine mesh	0.025	2	17.8 hours	35.6 hours
Filtered, coarse mesh	0.1	4	6.5 hours	26 hours

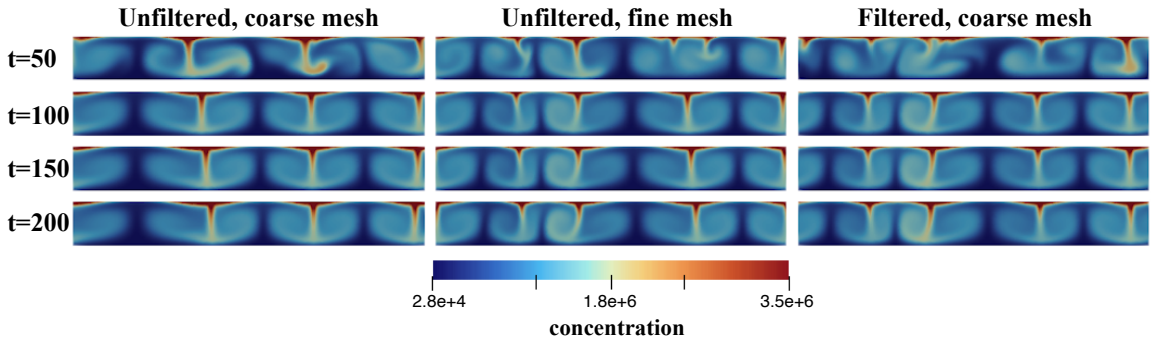

Fig. 7.7: Microorganism concentration fields for the concentration-dependent viscosity case at $t = 50, 100, 150, 200$. Columns from left to right: unfiltered method on the coarse mesh, unfiltered method on the fine mesh, adaptive filtered method on the coarse mesh. Up to a small horizontal phase shift induced by the periodic direction, the filtered coarse-mesh solution captures the dominant plume structures of the fine-mesh reference more accurately than the unfiltered coarse-mesh solution.

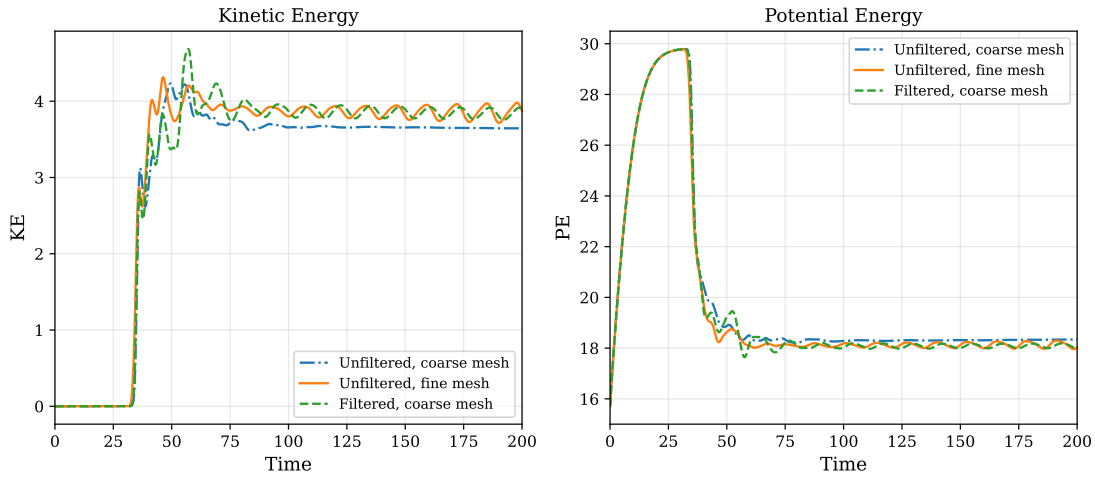

Fig. 7.8: Evolution of the kinetic energy $\mathrm{KE}(t)$ and potential energy $\mathrm{PE}(t)$ for concentration-dependent viscosity case. The adaptive filtered method on the coarse mesh closely follows the long-time energy behavior of the fine-mesh unfiltered reference.

Table 7.3: Computational cost for concentration-dependent viscosity case.

Method	Mesh size h	MPI ranks	Wall-clock time	Core-hours
Unfiltered, coarse mesh	0.1	2	2.25 hours	4.5 hours
Unfiltered, fine mesh	0.025	2	42.5 hours	85 hours
Filtered, coarse mesh	0.1	4	8.3 hours	33.2 hours

Figure 7.8 shows the corresponding kinetic and potential energies. The filtered method reproduces the main long-time energy behavior while requiring substantially fewer degrees of freedom. This indicates that the adaptive filtering remains effective beyond the constant viscosity setting.

Table 7.3 reports the computational cost of the three simulations. The unfiltered computation on a fine mesh is substantially more expensive in the concentration-dependent viscosity case than in the corresponding constant viscosity case. The filtered computation on a coarse mesh provides a more accurate approximation of the reference than the unfiltered simulation on the coarse mesh, while requiring significantly less wall-clock time than the unfiltered computation on the fine mesh.

8. Conclusions. In this work, we developed a spatially adaptive Leray-α regularized finite element method for geotactic bioconvection. The method reduces the computational cost while retaining key properties of the original model, including conservation of the total microorganism mass and the kinetic–potential energy balance. We established a stability estimate for the semi-discrete scheme and proved linear convergence of the decoupled subiterations under a time-step restriction. We also analyzed the grad-div stabilized adaptive filter at both the continuous and discrete levels. The analysis reveals a competing divergence-residual effect at the discrete level, providing a theoretical basis for selecting a suitable range of filter parameters.

Numerical simulations show that the filtered method on coarse meshes closely reproduces the dominant large-scale dynamics obtained by the standard unfiltered method on much finer meshes, with a substantial reduction in computational cost. Additional simulations with concentration-dependent viscosity demonstrate that the method remains effective in a nonlinear viscosity regime.

Several questions remain open. The present analysis identifies a suitable range of grad-div parameters but does not prescribe a universal optimal choice. In addition, the indicator function used here is adapted from the Navier–Stokes setting, and the development of indicators tailored specifically to bioconvection may further

improve the method. These directions will be investigated in our future work.

Funding. Martina Bukač is partially supported by the National Science Foundation under grants DMS-2208219, DMS-2205695 and DMS-2602215. Catalin Trenchea is partially supported by the National Science Foundation under grant DMS-2208220.

Data availability. The source code, input files, and post-processing scripts used to generate the numerical results in this study are maintained in a private GitHub repository during the review process and will be made publicly available upon publication.

REFERENCES

[1] M. Akbaş and A. Bowers, *Improving accuracy in the leray model for incompressible nonisothermal flows via adaptive deconvolution-based nonlinear filtering*, Math Meth Appl Sci., 44 (2021), pp. 6679–6699.
[2] S. Badia and F. Verdugo, *Gridap: An extensible Finite Element toolbox in Julia*, J. Open Source Softw, 5 (2020), p. 2520.
[3] G. Batchelor and J. Green, *The determination of the bulk stress in a suspension of spherical particles to order c^2*, J. Fluid Mech., 56 (1972), pp. 401–427.
[4] M. A. Bees, *Advances in Bioconvection*, Annu. Rev. Fluid Mech., 52 (2020), pp. 449–476.
[5] M. A. Bees and O. A. Croze, *Mathematics for streamlined biofuel production from unicellular algae*, Biofuels, 5 (2014), pp. 53–65.
[6] J. Bezanson, A. Edelman, S. Karpinski, and V. B. Shah, *Julia: A Fresh Approach to Numerical Computing*, SIAM Rev., 59 (2017), pp. 65–98.
[7] A. L. Bowers and L. G. Rebholz, *Numerical study of a regularization model for incompressible flow with deconvolution-based adaptive nonlinear filtering*, Comput. Methods Appl. Mech. Engrg., 258 (2013), pp. 1–12.
[8] J. Burkardt and C. Trenchea, *Refactorization of the midpoint rule*, Appl. Math. Lett., 107 (2020), p. 106438.
[9] Y. Cao, S. Chen, and H.-W. van Wyk, *Well-posedness and finite element approximation of time dependent generalized bioconvective flow*, Numer. Methods Partial Differential Equations, 36 (2020), pp. 709–733.
[10] A.-L. Cauchy, *Équations différentielles ordinaires*, Éditions Études Vivantes, Ltée., Ville Saint-Laurent, QC; Johnson Reprint Corp., New York, 1981. Cours inédit. Fragment.
[11] S. Childress, M. Levandowsky, and E. A. Spiegel, *Pattern formation in a suspension of swimming microorganisms: equations and stability theory*, J. Fluid Mech., 69 (1975), pp. 591–613.
[12] E. Colmenares, D. Sanhueza, and R. Ruiz-Baier, *Convergence analysis and adaptive computation of a Banach-space mixed finite element method for generalized bioconvective flows*, Comput. Methods Appl. Mech. Engrg., 456 (2026), p. 118964.
[13] R. de Aguiar, B. Climent-Ezquerra, M. A. Rojas-Medar, and M. D. Rojas-Medar, *On the Convergence of Galerkin Spectral Methods for a Bioconvective Flow*, J. Math. Fluid Mech., 19 (2017), pp. 91–104.
[14] M. Edwards, M. Bukač, and C. Trenchea, *A second-order partitioned method for bioconvective flows with concentration dependent viscosity*, Ann. Math. Sci. Appl., 9 (2024), pp. 141–184.
[15] G. P. Galdi and W. J. Layton, *Approximation of the larger eddies in fluid motions. II. A model for space-filtered flow*, Math. Models Methods Appl. Sci., 10 (2000), pp. 343–350.
[16] G. P. Galdi and B. Straughan, *Exchange of stabilities, symmetry, and nonlinear stability*, Arch. Rat. Mech. Anal., 89 (1985), pp. 211–228.
[17] A. V. Getling, *Rayleigh-Bénard convection: structures and dynamics*, vol. 11, World Scientific, 1998.
[18] S. Ghorai and N. Hill, *Periodic arrays of gyrotactic plumes in bioconvection*, Phys. Fluids, 12 (2000), pp. 5–22.
[19] S. Ghorai and N. A. Hill, *Development and stability of gyrotactic plumes in bioconvection*, J. Fluid Mech., 400 (1999), pp. 1–31.
[20] ———, *Gyrotactic bioconvection in three dimensions*, Phys. Fluids, 19 (2007), p. 054107.
[21] J.-L. Guermond, *On the use of the notion of suitable weak solutions in cfd*, Int. J. Numer. Meth. Fluids, 57 (2008), pp. 1153–1170.
[22] J.-L. Guermond, R. Pasquetti, and B. Popov, *From suitable weak solutions to entropy viscosity*, J. Sci. Comput., 49 (2011), pp. 35–50.
[23] J. G. Heywood and R. Rannacher, *Finite-element approximation of the nonstationary Navier-Stokes problem. IV. Error analysis for second-order time discretization*, SIAM J. Numer. Anal., 27 (1990), pp. 353–384.
[24] JuliaCollections and contributors, *Datastructures.jl*, 2023. Version v0.18.22.
[25] E. L. Koschmieder, *Bénard cells and Taylor vortices*, Cambridge University Press, 1993.
[26] I. M. Krieger, T. J. Dougherty, et al., *A mechanism for non-newtonian flow in suspensions of rigid spheres*, Trans. Soc. Rheol, 3 (1959), pp. 137–152.
[27] O. A. Ladyženskaja, *Solution "in the large" to the boundary-value problem for the Navier-Stokes equations in two space variables*, Dokl. Akad. Nauk SSSR, 123 (1958), pp. 427–429.
[28] W. Layton, *Introduction to the numerical analysis of incompressible viscous flows*, SIAM, 2008.
[29] W. Layton, L. G. Rebholz, and C. Trenchea, *Modular nonlinear filter stabilization of methods for higher reynolds numbers flow*, J. Math. Fluid Mech., 14 (2012), pp. 325–354.
[30] W. Layton and S. Xu, *Conditioning of linear systems arising from penalty methods*, Electron. Trans. Numer. Anal., 58 (2023), pp. 394–407.
[31] J. Leray, *Sur le mouvement d'un liquide visqueux emplissant l'espace*, Acta Math., 63 (1934), pp. 193–248.

[32] J. MANYER, A. F. MARTÍN, AND S. BADIA, *Gridapsolvers.jl: Scalable multiphysics finite element solvers in Julia*, J. Open Source Softw, 9 (2024), p. 7162.
[33] A. M. MIL-MARTÍNEZ, R. O. VARGAS, A. GÓMEZ-LÓPEZ, A. ZACARÍAS, J. P. ESCANDÓN, E. GARCÍA-LEAL, AND R. MIL-MARTÍNEZ, *Numerical Simulation of Gravitactic Bioconvection with Nanoparticles: An Application of Solids Removal in Wastewater Using a Thermal Source*, Micromachines, 16 (2025), p. 553.
[34] M. MOONEY, *The viscosity of a concentrated suspension of spherical particles*, J. Colloid Sci., 6 (1951), pp. 162–170.
[35] J. NIE, M. BUKAČ, AND C. TRENCHEA, *Stability of geotactic bioconvection: Analytical bounds and numerical thresholds*, SIAM Journal on Life Sciences., (2026). in press.
[36] T. J. PEDLEY, N. A. HILL, AND J. O. KESSLER, *The growth of bioconvection patterns in a uniform suspension of gyrotactic micro-organisms*, J. Fluid Mech., 195 (1988), pp. 223–237.
[37] M. S. PLESSET AND H. WINET, *Bioconvection patterns in swimming microorganism cultures as an example of Rayleigh–Taylor instability*, Nature, 248 (1974), pp. 441–443.
[38] P. SAGADEVAN, U. RAJU, M. MURUGESAN, U. FERNANDEZ-GAMIZ, AND S. NOEIAGHDAM, *Chemical reactions with the Casson nanofluid flow by the bioconvective behavior of microorganisms over a spinning disc*, Heliyon, 11 (2025), p. e41238.
[39] R. ŠIMKUS, *Bioluminescent monitoring of turbulent bioconvection*, Luminescence, 21 (2006), pp. 77–80.
[40] A. TAKHIROV AND C. TRENCHEA, *Efficient nonlinear filter stabilization of the Leray-α model*, J. Comput. Phys., 471 (2022), p. 111668.
[41] M. VAN REEUWIJK, H. J. J. JONKER, AND K. HANJALIĆ, *Applying the Leray-α model to Rayleigh–Bénard convection*, in Progress in Turbulence II, vol. 109 of Springer Proceedings in Physics, Springer, Berlin, Heidelberg, 2007, pp. 197–200.
[42] M. VAN REEUWIJK, H. J. J. JONKER, AND K. HANJALI'C, *Leray-α simulations of wall-bounded turbulent flows*, Int. J. Heat Fluid Flow, 30 (2009), pp. 1044–1053.
[43] F. VERDUGO AND S. BADIA, *The software design of Gridap: A Finite Element package based on the Julia JIT compiler*, Comput. Phys. Commun., 276 (2022), p. 108341.